An evaluation of size-resolved cloud microphysics scheme numerics for use with radar observations
Part II: Condensation and evaporation

Hyunho Lee[1,2], Ann M. Fridlind[2], and Andrew S. Ackerman[2]

[1] Department of Atmospheric Science, Kongju National University, Gongju, South Korea

[2] NASA Goddard Institute for Space Studies, New York, NY 10025, U.S.A.

Journal of the Atmospheric Sciences

Submitted July 2020

Revised November 2020

Revised February 2021

Corresponding author: Hyunho Lee, Department of Atmospheric Science, Kongju National University, Gongju, Chungcheongnam-do 32588, South Korea

E-mail address: hyunho.lee@kongju.ac.kr

Abstract

Accurate numerical modeling of clouds and precipitation is essential for weather forecasting and climate change research. While size-resolved (bin) cloud microphysics models predict particle size distributions without imposing shapes, results are subject to artificial size distribution broadening owing to numerical diffusion associated with various processes. Whereas Part 1 addressed collision-coalescence, here we investigate numerical diffusion that occurs in solving condensation and evaporation. In a parcel model framework, all of the numerical schemes examined converge to one solution of condensation and evaporation as the mass grid is refined, and the advection-based schemes are recommended over the reassigning schemes. Including Eulerian vertical advection in a column limits the convergence to some extent, but that limitation occurs at a sufficiently fine mass grid, and the number of iterations in solving vertical advection should be minimized to reduce numerical diffusion. Insubstantial numerical diffusion in solving condensation can be amplified if collision-coalescence is also active, which in turn can be substantially diminished if turbulence effects on collision are incorporated. Large-eddy simulations of a drizzling stratocumulus field reveal that changes in moments of Doppler spectra obtained using different mass grids are consistent with those obtained from the simplified framework, and that spectral moments obtained using a mass grid designed to effectively reduce numerical diffusion are generally closer to observations. Notable differences between the simulations and observations still exist, and our results suggest a need to consider whether factors other than numerical diffusion in the fundamental process schemes employed can cause such differences.

1. Introduction

Simulating, understanding, and predicting cloud development and precipitation formation using numerical models has been of great interest in recent decades because clouds and precipitation significantly affect not only daily weather but also water resource circulation and climate change at the global scale. Despite great interest and effort, however, clouds and precipitation remain widely accepted as leading sources of ample uncertainties in projecting future climate change, indicating that further efforts are essential.

Many operational purposes are fulfilled if a numerical cloud model provides basic macrophysical properties such as cloud fraction, cloud optical depth, and precipitation rate. Bulk microphysical models, which predict hydrometeor mixing ratios and perhaps number concentrations based usually on prescribed particle size distribution shapes, can efficiently provide such macrophysical properties, and hence have been widely utilized for research and operational purposes. However, more detail is sometimes necessary to study complex physical processes that occur in clouds, and also to predict cloud properties more accurately. For example, the detailed spatiotemporal evolution of hydrometeor size distributions, which cannot be generally simulated using a bulk microphysics model, are vital for understanding stratocumulus because they substantially impact precipitation development and radiative forcing. An Eulerian size-resolved ("bin") cloud microphysics model can represent such evolution of particle size distributions by dividing the complete size range of cloud and precipitation drops into dozens or hundreds of mass bins and predicting cloud particle number concentration in each size bin, whereas a typical bulk model adopts prescribed size distribution functions. A bin microphysics model can therefore be especially useful for predicting detailed and generally more accurate information on the evolving shapes of hydrometeor size distributions (e.g., Khain et al. 2015, and references therein), and is a

tool used to develop bulk microphysics parameterizations (e.g., Khairoutdinov and Kogan 2000; Seifert and Beheng 2001; Lee and Baik 2017).

Despite this valuable capability, however, bin microphysics models are prone to artificial broadening of particle size distributions associated with the numerical schemes used to represent various processes (e.g., Cooper et al. 1997; Khain et al. 2000; Morrison et al. 2018). Since most bin microphysics models use a fixed discrete mass grid whereas the masses of cloud particles vary continuously from microphysical processes, a bin model must remap those cloud particles with arbitrary masses onto its fixed mass grid. The artificial broadening occurs during this remapping process; some degree of numerical diffusion is therefore unavoidable in principle.

Many bin microphysics modeling studies have sought to assess and minimize the numerical diffusion. Some have proposed new numerical schemes to treat microphysical processes with greater accuracy (e.g., Kovertz and Olund 1969; Egan and Mahoney 1972; Berry and Reinhardt 1974; Liu et al. 1997; Bott 2000; Wang et al. 2007; Khain et al. 2008), and others have made extended assessments of existing scheme numerics (e.g., Seeßelberg et al. 1996; Wang et al. 2007; Grabowski et al. 2011; Lee et al. 2019). In the Part I of this study (Lee et al. 2019), motivated by poor agreement of forward-simulated W-band radar Doppler spectra from large-eddy simulation (LES) results using a bin microphysics scheme, we evaluated three numerical schemes designed to solve the stochastic collection equation, which is the governing equation of collisional growth of hydrometeors. We presented a scheme and a bin grid that could be used satisfactorily for simulating weakly drizzling stratocumulus, including negligible artificial broadening associated with collision-coalescence numerics for the purposes of calculating cloud radar Doppler spectra.

In this study, we extend our previous study to deal with condensation and evaporation in a bin microphysics model. Whereas artificial broadening during treatment of collision-coalescence

was especially apparent in comparison of simulated and observed Doppler spectra, Morrison et al. (2018, hereafter M18) pointed out that numerical diffusion from solving condensation is also substantial when condensation is combined with vertical advection. They reported that only reducing vertical grid spacing enough to resolve sharp vertical gradients, not better vertical advection schemes or finer bin grid refinements, is successful in obtaining a reasonable solution compared to that obtained using a Lagrangian cloud model. There are some distinct differences between this study and M18. Here we focus first on convergence of several schemes designed to solve condensation using a single-moment bin microphysics approach in a parcel model framework, which contrasts with M18 that mainly uses a double-moment bin model. Single-moment bin models are usually regarded as flexible for fundamentally altering the bin grid structure, which can influence numerical properties, as shown below. In addition, we examine convergence when including additional processes in the parcel model: condensation and collision-coalescence operating simultaneously, as well as evaporation. Finally, we conduct a series of 3-D simulations for lightly drizzling stratocumulus using a revised version of our LES model coupled with bin microphysics (from Part I), and examine characteristics of drop size distributions (DSDs). That examination is again done by comparing cloud radar Doppler spectra observed from a W-band Doppler radar with those obtained using a forward simulator as demonstrated in Part I.

Descriptions of condensation and evaporation in a bin microphysics model, as well as the numerical schemes examined in this study, are provided in section 2. Results obtained using a parcel and a column model are presented in section 3, and those obtained using an LES model in section 4. A summary and conclusions are given in section 5.

2. Condensation and evaporation in a bin microphysics model

Solving condensation and evaporation in a bin model usually consists of two steps. First, the rates of mass change of all cloud particles in regularly spaced bins are calculated. If steady-state molecular diffusion is assumed, the rate of mass change of drops from condensation and evaporation can be approximated as (e.g., Rogers and Yau 1989; Pruppacher and Klett 1997)

$$\frac{dm}{dt} = \frac{4\pi r v_F}{F_D + F_K}\left(S - \frac{a}{r} + \frac{br_N^3}{r^3 - r_N^3}\right), \quad (1)$$

where m and r are the mass and radius of cloud drops, v_F is the ventilation factor usually expressed as a function of the sedimentation Reynolds number, F_D and F_K are coefficients related to the vapor and heat diffusion, respectively, S is the environmental (i.e., grid-scale) supersaturation, r_N is the radius of dry aerosol, and a and b are coefficients related to the curvature and solute effects, respectively. Integrating this equation forward in time, cloud particles realize continuously evolving masses that deviate from those of the discrete model bins. As a second step, the cloud particles are then reassigned to the discrete bins. The first step is generally associated with physics rather than with numerics; although some studies have suggested computational improvements (e.g., Khain and Sednev 1996; Khain et al. 2008) and while those are worth examining, they are beyond the scope of this study. The second step, referred to hereafter as "renormalization", is the main source of numerical diffusion and is the focus in this study.

Several schemes have been proposed to solve the renormalization step in condensation and evaporation. They can be largely classified into two groups, one reassigning intermediate-mass particles to discrete bins while conserving specified moments, and the other treating renormalization as the advection of cloud particles along the mass axis. For schemes in the first group, it is straightforward to show that cloud particles that have the same mass must be reassigned into n bins if n moments are to be conserved. Although such schemes can strictly conserve more than one moment during the renormalization step, they encounter two fundamental problems that

can be readily demonstrated mathematically. First, all moments higher than the highest conserved moment must be overestimated, and overestimation is larger as the order of the moment is higher. This holds even if a scheme minimizes errors across several lower moments rather than strictly conserving them (e.g., Liu et al. 1997), revealing that numerical diffusion is substantial if such schemes are employed. In addition, if a scheme reassigns cloud particles into more than two bins to conserve more than two moments, it must yield a negative rate of change of number concentration at some bins, and to avoid a negative concentration, some ad hoc numerical treatments are necessary, which reduce numerical accuracy.

The schemes in the second group are essentially the same as typical Eulerian advection schemes along a spatial axis. Cloud particles at a specific time and location must move in one direction along the size axis during condensation or evaporation. Therefore, the only requirements on such schemes are numerical stability and positive definiteness. However, one clear disadvantage of the advection schemes is that they can conserve only one moment if they are applied in single-moment bin microphysics models. Typical schemes choose number concentration as the conserved moment because it does not vary during condensation or evaporation except for complete evaporation of small droplets. This means that all the other moments, such as cross section, mass concentration, and radar reflectivity, would develop errors while solving the renormalization step using these schemes. In particular, to conserve total water mixing ratio, the water vapor mixing ratio is recalculated after the renormalization step.

In this study, we examine two reassignment schemes and two advection schemes to solve the renormalization step. The first reassignment scheme distributes cloud particles that should be reassigned to the discrete bins into two adjacent bins to exactly conserve their number and mass ("2MOM" hereafter, Kovertz and Olund 1969). In this scheme, if N cloud particles whose mass is

160 M are reassigned to the ith and i+1th bins, the resultant number concentrations in the two bins n_i
161 and n_{i+1} are

162 $$n_i = N\frac{m_{i+1}-M}{m_{i+1}-m_i} \quad \text{and} \quad n_{i+1} = N\frac{M-m_i}{m_{i+1}-m_i}, \tag{2}$$

163 where m_i and m_{i+1} are the masses of the two adjacent bins which satisfy $m_i < M < m_{i+1}$. The other
164 reassigning scheme conserves three moments, which are number, mass, and Rayleigh-regime radar
165 reflectivity, by distributing cloud particles into three consecutive bins ("3MOM" hereafter, Khain
166 et al. 2008). The basic calculation principle of the 3MOM scheme is similar to that of the 2MOM
167 scheme. As mentioned above, however, the 3MOM scheme always induces a decrease in number
168 concentration at one of the three bins, which can cause negative concentrations. A simple method
169 that utilizes number concentrations of adjacent bins is adopted in this study to prevent negative
170 concentrations.

171 One advection scheme examined in this study is the piecewise parabolic method ("PPM"
172 hereafter, Colella and Woodward 1984) and the other is the Bott scheme (Bott 1989). Both
173 schemes are forward-in-time and positive definite, and calculate upwind fluxes. To achieve
174 numerical stability in the advection schemes, a time step is divided into substeps so that the
175 Courant-Friedrichs-Lewy (CFL) number along the size axis does not exceed unity. The Bott
176 scheme is slightly modified for grids with irregular spacing. Note that some numerical limiters can
177 be applied to advection schemes to keep the schemes monotonic (e.g., Colella and Woodward
178 1984), but those limiters are not considered in this study because of a possible increase in
179 numerical diffusion.

180 It should be noted that all of the schemes examined are suitable for a single-moment bin
181 microphysics model, which was selected for this study as described in the introduction. M18 used
182 a modified version of the top-hat method (Egan and Mahoney 1972), suitable for a double-moment

model and found it much less diffusive than a method for a single moment bin model (MPDATA, Smolarkiewicz 2006). We only consider single-moment bin models here because they can be readily used to examine convergence with respect to size bin grid refinement. The results will be compared with those of M18, which uses a double-moment bin model.

3. Parcel and column models

a. Condensation

A parcel model is first used to examine performance of the renormalization schemes solving condensation (i.e., convergence with respect to bin grid refinement). Condensation is the only microphysical process considered. We use a model setup identical to that of M18. The initial temperature, pressure, and relative humidity are 15°C, 900 hPa, and 100.6%, respectively. Parcel vertical velocity is fixed at 1 m s^{-1} throughout the integration. The temperature and pressure are updated based on adiabatic expansion assuming hydrostatic equilibrium. Condensation affects air temperature and humidity. The drop number concentration per unit air density[1] is 50 mg^{-1}, which is the same value as the smaller aerosol number concentration case of M18 that reflects clean (i.e., not polluted) clouds. The initial DSD has a constant dN/dr value within a radius range of r = 1–3 μm, corresponding to a standard deviation of 0.5 μm. The dynamic model time step is 5 s. In solving condensation, the rate of change of drop mass is calculated with a time step of 0.1 s, and the renormalization step is calculated once per dynamic model time step. The model is integrated for 10 min. Attributable to the initial supersaturation and the prescribed vertical velocity, only

[1] We note that the number of particles per unit air mass can be referred to as the particle number mixing ratio or the number concentration of particles per unit air density. In this study, it will be simply referred to as the number concentration hereafter.

condensation occurs throughout the integration, so the drop number concentration does not change and the drop mass mixing ratio increases monotonically.

First the model simulation is run with a typical geometric bin grid, in which the radii of two consecutive bin grids are expressed as

$$r_{i+1} / r_i = 2^{1/(3s)}, \quad (3)$$

where s controls the bin grid refinement in a geometric bin grid. The masses of bins are then doubled every s bins. The parameter s is set to 2, as in the large eddy simulations of Lee et al. (2019).

In addition to the typical bin grids that have fixed masses throughout the integration, we also utilize an alternative bin grid in which bin masses vary dynamically. In this bin grid, the mass of each bin at the initial time is identical to that in the geometric bin grid described above, but evolves every time step according to change of mass owing to condensation. Thus, no renormalization is needed and results are equivalent to those of a Lagrangian scheme, essentially free of numerical diffusion. This grid will be called the dynamic grid hereafter, and the solution obtained using the dynamic grid will be regarded as the reference solution hereafter. Note that not only the mass but also all other bin-related quantities such as terminal velocity also evolve together in the dynamic grid.

Figure 1 shows the DSD at the end of each parcel model simulation obtained using different renormalization schemes. The reference solution DSD becomes so narrow that the final difference in radii between the largest (99th percentile) and smallest (1st percentile) drops is only 0.2 μm. This narrowing is a well-known characteristic of the condensation process, wherein the growth rate of drop radius slows as its radius grows. However, all of the renormalization schemes yield substantial numerical diffusion compared to the reference solution. The 2MOM scheme yields the

widest DSD, or in other words, the greatest numerical diffusion. The other three schemes exhibit performance somewhat better than the 2MOM scheme. The 3MOM scheme yields a DSD that has a relatively long tail at the large drop side compared to the other two advection schemes, and such skewness is most noticeable in the Rayleigh-regime reflectivity factor as a function of drop fall speed, which is an idealization of a Doppler spectrum measured by cloud radar.

Figure 2 shows time series of DSD characteristics obtained from the same simulations. Note that the temporal evolution of DSD characteristics from the reference simulation is almost the same as that of the benchmark run of M18 (see their Fig. 8). The median drop radius does not vary much across renormalization schemes (Fig. 2a), so the differences in DSD width (Fig. 2c) are mainly attributable to differences in the largest drop sizes (Fig. 2b). The DSD standard deviation, which is another metric of DSD width, is generally smoother but shows a temporal trend very similar to the difference between the largest radius and the median radius. The reference simulation yields a continuously narrowing DSD, as mentioned above. However, all of the renormalization schemes fail to simulate such a narrowing DSD except at the very first stage of the simulations. Instead, DSD widths continuously increase in all the schemes. As shown in Fig. 1, the 2MOM scheme develops the largest DSD width, almost twice those obtained using the other schemes.

To examine whether this continuous increase in DSD width is at least partially associated with progressively increasing bin width, a characteristic of geometric grids, we introduce another grid in which bin radii increase linearly, which is expressed as

$$r_{i+1} - r_i = 1/d \ \mu\text{m}, \tag{4}$$

where d controls the grid refinement. Figure 3 shows time series of DSD characteristics obtained using the linear mass grid with d = 1 (i.e., the difference in radii between two adjacent bins is constant at 1 μm). The increasing DSD width with time shown in Fig. 2 almost vanishes in Fig. 3,

and the DSD widths shown in the standard deviation remain almost constant at approximately ~1 μm except for the 2MOM scheme. Note that the standard deviations of DSD from the 3MOM, PPM, and Bott schemes are similar to the bin width, which implies that the DSD width might be restricted by the bin width in this experimental setting, as also pointed out in M18.

Convergence of DSD width with respect to bin grid refinement is next examined on both linear and geometric bin grids. Figure 4 shows the largest drop radius and standard deviation of DSD at the end of the model integration obtained from various bin grids and different renormalization schemes. Here the maximum allowed drop radius is set to ~40 μm in all bin grids. A linear bin grid and a "corresponding" geometric bin grid, which uses the same number of bins to cover the given radius range, are compared in the figure. For instance, a total of 80 bins are used both in the linear bin grid with d = 2 and in the geometric bin grid with s = 5. Note that if both grids cover the same radius range of ~40 μm as here, a linear bin grid has smaller bin width than a corresponding geometric grid beyond a bin at which the radius is ~11 μm. While all of the renormalization schemes yield solutions that converge to the reference solution as the bin grid is refined, a linear bin grid always yields smaller DSD width than does the corresponding geometric bin grid. This difference suggests that a linear bin grid is more efficient than a geometric bin grid in accurately solving condensation, attributable to the smaller bin width at common drop radii (beyond ~11 μm in this setup). Note that although the reverse is true at the small droplet region, condensation there is so fast that small droplets would grow very quickly beyond the threshold radius in which a linear grid is more efficient. The number of bins that the initial DSD occupies is greater in a geometric bin grid than in a linear bin grid, but the later bin widths are more important in reducing numerical diffusion during condensation.

271 Note that although all of the renormalization schemes converge, how narrow bin width
272 must be in order to obtain a sufficiently accurate solution depends on the convergence criterion.
273 Furthermore, numerical diffusion from solving condensation might be more problematic when
274 combined with Eulerian vertical advection and/or collision-coalescence, as explored in the
275 following sections.
276
277 *b. Condensation with vertical advection*
278 We next consider a column model to treat Eulerian vertical advection and condensation
279 simultaneously. The model setup is again almost identical to that of M18. The thermodynamic
280 state and DSD in the lowest layer are the same as in the parcel setup described above and do not
281 vary during model integration. The thermodynamic state in the overlying layers also varies
282 following the parcel model result. The vertical grid spacing is 10 m unless otherwise specified,
283 different from the default value used in M18 (20 m), and the model top height is 600 m. The
284 vertical velocity is 1 m s^{-1} in all layers throughout the model integration. To evaluate the vertical
285 advection of potential temperature and humidity, an advection scheme that uses a fifth-order
286 spatial differentiation to evaluate a flux at each cell boundary and a third-order Runge Kutta (RK3)
287 scheme in time is used (Wicker and Skamarock 2002), as in M18. However, a flux limiter that
288 forces the advection scheme to be positive definite or monotonic is not applied. To evaluate the
289 vertical advection of drops, the PPM scheme with a first-order forward-in-time approach is used.
290 Drop sedimentation and collisions are neglected. The dynamic model time step and the time step
291 for evaluating the rate of change of drop mass from condensation are 5 and 0.1 s, respectively, as
292 in the parcel experiments. The model approaches a steady state after ~10 min, which is the time

293 required for drops from the lowest layer to reach the model top, so the model is integrated for 15
294 min and the resulting equilibrium examined.

295 Figure 5a–d shows the results obtained using various renormalization schemes with a
296 linear mass grid of $d = 1$ in the column model. Compared to Fig. 3, it is shown that except in the
297 lowest few layers, the column model results are almost the same as for the parcel model, which
298 indicates that the column model is a faithful version of the parcel model in this model configuration.
299 The relatively greater DSD width in the lowest few layers of the column model compared to that
300 of the parcel model is apparently attributable to a non-physical reason explained by M18: in the
301 parcel model all of the drops ascend together while they grow, whereas in the column model
302 generally only a portion of the drops in any specific layer ascend owing to the characteristics of
303 Eulerian advection schemes. The remaining drops in that layer then grow by condensation and
304 smaller drops also reach that layer from below, which causes artificial broadening of DSD. By
305 comparing Fig. 5a–d to Fig. 3, vertical advection is seen to have little impact on the numerical
306 diffusion from solving condensation in this model configuration.

307 Figure 5e–h shows the results obtained using the PPM scheme for the renormalization step
308 with progressively increasing bin grid refinement. The DSD spectral widths decrease with finer
309 bin grids, converging to effectively match the reference solution when $d = 4$, with an ever
310 diminishing degree of improvement as d increases further. This behavior presents a contrast to the
311 parcel results, for which convergence is not effectively reached until $d = 16$. In other words, the
312 column model never gets close to the parcel model that continuously reduces the DSD spectral
313 width with finer bin refinement. This is similar to M18's results, where the DSD width also
314 converges to a value that is much greater than that obtained from their benchmark simulation. In
315 this study, the DSD width measured as the difference between the largest and the median drop

316 radius converges slightly below 1 μm, which is almost the same as M18 obtained using the vertical
317 grid spacing same as that of this study (10 m). Note that the DSD width converged when *d* is ~ 0.5
318 in M18 but ~ 4 in this study, presumably owing to the relatively smaller numerical diffusion in
319 double-moment microphysics models than that in single-moment models.

320 Figure 6 shows convergence of the solutions with respect to bin grid refinement obtained
321 using the PPM scheme. Each DSD standard deviation converges to a certain value as vertical
322 height increases for a specific model configuration (c.f., Fig. 5), and the converged value is shown
323 in the figure. Whereas M18 clearly contrasted the results from the parcel and the column model
324 and presented convergence of DSD broadening with respect to vertical grid spacing in the column
325 model, this study depicts how the column model yields the results different from the parcel results
326 with respect to bin grid refinements. The column model always stops converging at a specific bin
327 grid refinement, whereas the parcel model shows continuously decreasing numerical diffusion
328 with finer grids. This difference suggests that the column model's Eulerian vertical advection is
329 limiting convergence. Sensitivity tests with different vertical grid spacing and model time steps
330 indicate that the dependency on vertical grid spacing is much greater than that on model time step
331 length, as also pointed out in M18. However, it is shown that such limitations occur at a coarser
332 bin grid and are further from converged with increasing vertical grid spacing, surprisingly, with
333 decreasing model time step length.

334 While M18 suggested that the role of time step length in modulating DSD width is not
335 clear, Fig. 6 reveals that a shorter model time step worsens convergence across these simulations.
336 This is because as the CFL number in vertical advection decreases, the number of iterations for
337 advection calculation increases, which generally enhances numerical diffusion. Note that if a first-
338 order forward-in-time scheme with a CFL number of exactly unity is used, the column model result

is effectively identical to the parcel model result (not shown, see also M18). However, it should be noted that a CFL number of exactly unity is practically almost impossible to achieve in a typical cloud simulation in which vertical velocity varies, and furthermore, a shorter model time step length is usually preferred to improve overall model accuracy.

When the time integration method of vertical advection scheme is changed from a first-order forward-in-time to an RK3, although an RK3 is known to be more stable (i.e., stable at a larger CFL number) and generally more accurate than a first-order forward-in-time method, the DSD width converges at a greater value. This is mainly owing to the increased number of iterations from one to three per model time step.

c. Condensation and collision-coalescence

M18 diagnosed the effects on collision-coalescence of numerical diffusion from solving condensation. In this study, rather than diagnose, we directly include drop collision-coalescence in the parcel model. Following Lee et al. (2019), the exponential Bott collection scheme (Bott 2000) is applied to solve the stochastic collection equation. The collision efficiencies assembled by Hall (1980) are used, and the coalescence efficiency is assumed to be unity. The terminal velocities of drops provided by Beard (1976) are used to construct the hydrodynamic collection kernel, but transport by drop sedimentation is neglected in the parcel model framework. A constant vertical velocity of 1 m s^{-1} is applied for the first 10 min, and it drops to zero after that. The model is integrated for 1 h. All the other model configurations are identical to those in the condensation experiments.

In order to take advantage of a linear bin grid for solving condensation but also span a wide range of drop radii with fewer bins, we implement a new bin grid, in which linear and geometric

bin grids are mixed, analogous to a vertical spatial grid that is stretched with distance from the surface. In this bin grid, the difference in radii between two consecutive bins is constant until the drop radius reaches a certain threshold value, at which point that difference then increases geometrically, which is expressed as

$$r_{i+1} - r_i = \begin{cases} 1/d \ \mu\text{m} & \text{if } r_i \le r_c \\ 2^{1/(3s)} \times \left(r_i - r_{i-1}\right), & \text{if } r_i > r_c \end{cases}, \tag{5}$$

A sample set of the grid spacing as a function of radius is shown in Fig. 7. It can be readily shown that m_{i+1} / m_i asymptotically approaches $2^{1/s}$ in the geometric grid. This bin grid avoids discontinuity in bin width, which would occur if the linear bin grid and a typical geometric bin grid were more simply combined. The threshold radius r_c is set to 25 μm.

Figure 8 shows the time evolution of size distributions of number, mass, and reflectivity of drops obtained using the mixed grid with the PPM renormalization scheme, as well as the dynamically moving grid in solving condensation without any renormalization scheme. Note that the collection scheme used in this study works at any (irregular) bin grid without altering the grid. In the mixture grids, only d in (5) is varied, with values of 1, 4, and 16, and s is fixed at 2, based on the convergence test of collection schemes documented by Lee et al. (2019). Distinct differences are seen in a relatively earlier model integration period when t < 30 min, and the results from different bin grid refinements are similar to each other when t > 35 min. When t < 30 min, initial drizzle drops with radius of ~40–100 μm are clearly more abundant as the bin grid is coarser. Furthermore, such earlier formation of drizzle drops compared to the dynamically moving bin grid is clearly seen even with a very fine bin grid (d = 16), in which the number of bins is greater than 400. Given that the difference in condensation-driven DSD width broadening between the linear grid with d = 16 and the dynamic grid is minimal (Fig. 4), this time evolution of DSD reveals that even such a small difference can cause a relatively clear difference when collision-coalescence is

385 also considered, and that the initial drizzle formation in a numerical model is substantially sensitive
386 to DSD shape.

387 Integral quantities of DSDs observed by a Doppler cloud radar are calculated from the bin
388 microphysics model output. We use McGill Radar Doppler Spectra Simulator (MRDSS, Kollias
389 et al. 2014; Rémillard et al. 2017) to compute DSD quantities with the parameter set for a 95 GHz
390 W-band cloud radar. The MRDSS forward simulator calculates the backscatter cross section of
391 drops using Mie theory. Figure 9 shows the time evolution of DSD quantities with different bin
392 grid refinements. Here the sign of Doppler velocity is defined to be positive if a drop ascends.
393 Because all the simulations are run with a prescribed vertical velocity that is zero after t = 10 min,
394 the Doppler velocity is always negative owing to the defined drop fall velocity although explicit
395 sedimentation is not considered. We would therefore say that the Doppler velocity increases when
396 it has a more negative value.

397 All the simulations exhibit the common trend of DSD quantities: at a relatively early stage
398 (between 15 and 20 min), DSDs start to skew negatively (i.e., elongated to the large drop tail) and
399 become wider. When the DSD skewness reach a minimum value, the mean Doppler velocity starts
400 to increase. Climbing from its minimum, the DSD skewness then increases towards a positive
401 value, while the DSD width reaches a local maximum by the time skewness crosses zero. From its
402 maximum value, the skewness then decreases slowly but remains positive, while the DSD width
403 seems to converge to a specific value and the rates of monotonically increasing reflectivity and
404 mean Doppler velocity are generally decelerated.

405 The simulation with a coarser bin grid yields an earlier increase in the total reflectivity
406 factor and the mean Doppler velocity, as expected owing to earlier formation of drizzle caused by
407 numerical diffusion in condensation. The maximum time difference compared to the reference

408 solution is ~5 min when d = 1 and ~1 min when d = 16. Such a time difference is also seen in the
409 time series of DSD width and skewness. While the reflectivity factor and Doppler velocity seem
410 to show time difference only, the DSD width and skewness show clear differences other than
411 timing depending on bin grid refinement. As the bin grid is coarser, the minimum DSD skewness
412 is less negative, the DSD skewness at a later stage is less positive, and the local maximum of DSD
413 width is smaller or nonexistent.

414 To see whether the numerical diffusion from solving condensation leaves unique traces on
415 DSD evolution other than a simple timing difference, DSD quantities are depicted again but as a
416 function of reflectivity (Fig. 10), which is readily derived from Doppler cloud radar output (e.g.,
417 Rémillard et al. 2017; Lee et al. 2019). Although the DSD quantities are arranged as a function of
418 reflectivity rather than of time, the experiments with finer bin grids yield more negative DSD
419 skewness under a relatively low reflectivity and wider and more positively skewed DSD under a
420 relatively high reflectivity. Furthermore, such differences to the reference solution are clearly seen
421 even with a very fine bin grid (d = 16). Therefore, it appears that numerical diffusion from solving
422 condensation affects not only the timing of drizzle onset but also DSD characteristics during DSD
423 evolution, and these effects can be pronounced even with minimal numerical diffusion.

424 Recently, some studies have suggested that turbulence in clouds can affect cloud
425 development in many ways. Among them, some have shown that turbulence can accelerate large
426 drop formation by accelerating the rate of collisions between drops, particularly between drops
427 with similar sizes (Ayala et al. 2008; Franklin 2008; Pinsky et al. 2008a; Wang and Grabowski
428 2009; Seifert et al. 2010; Wyszogrodzki et al. 2013; Lee et al. 2015; Witte et al. 2019). Therefore,
429 the effects of numerical diffusion from solving condensation might be reduced when including
430 turbulence-induced collision enhancement (TICE). To examine this possibility, we conduct

another series of experiments with the same parcel model but now including TICE. Here the turbulent collision kernel of Ayala et al. (2008) and Wang and Grabowski (2009) is incorporated in the parcel model, similar to Seifert et al. (2010) and Witte et al. (2019). The turbulent kinetic energy dissipation rate is fixed to 50 $cm^2\ s^{-3}$ throughout the model integration.

Figure 11, which is the same as Fig. 10 but for the simulations including TICE, shows that there still remain distinct differences in DSD width and skewness between the bin microphysics model and the dynamic parcel model. However, those differences considerably diminish when including TICE. In addition to TICE, turbulence is hypothesized to broaden DSDs at an early (i.e., condensation-dominant) stage of cloud development by causing spatiotemporal supersaturation fluctuations (e.g., Abade et al. 2018; Pardo et al. 2020). Thus, including turbulence may reduce the effects of numerical diffusion from solving condensation on simulated cloud development.

d. Evaporation

Finally, performance of the renormalization schemes in solving evaporation is also briefly examined. The same parcel model is used. The initial relative humidity is 99.5%, and the vertical velocity is set to –0.5 m s^{-1}. The initial DSD follows the Marshall-Palmer distribution, which is expressed as a simple exponential function, with a rain rate of 1 mm h^{-1}. The initial temperature and pressure are the same as those in the condensation experiment. The model is integrated for 20 min. If the mass of a certain bin reduces by evaporation and becomes smaller than the smallest mass of a given bin grid, the number concentration at the corresponding bin is set to zero before solving the renormalization step.

Figure 12 shows the DSDs at the end of model integration obtained using the different renormalization schemes with a geometric bin grid of $s = 2$. The reference simulation, which adopts

454 the dynamic bin grid, reveals that the smallest drop size is ~100 μm depending on model time step,
455 whereas all the renormalization schemes yield DSDs extended to the smallest drop size. However,
456 the differences in small droplets are almost negligible in size distributions of mass and radar
457 reflectivity (Figs. 12b–d). The 2MOM scheme obviously overestimates mass and radar reflectivity
458 of drops, but the other three schemes show results quite similar to those of the reference solution
459 even in this relatively coarse bin grid. The 3MOM scheme shows a zigzagging DSD at the small
460 drop tail, which might be caused by the ad hoc method used to prevent negative number
461 concentrations. The PPM scheme also yields some zigzagging of DSD in the radius range of ~500
462 μm (visible primarily in the higher moments) attributable to excluding a monotonic limiter, but it
463 diminishes as the bin grid is further refined (not shown).

464 Convergence of the renormalization schemes in solving evaporation is examined. Figure
465 13 shows the drop number concentration and drop mixing ratio at the end of the model integration
466 with various bin grids and different renormalization schemes. Only geometric bin grids are used
467 and linear bin grids are excluded because a linear bin grid requires too many bins to cover a wide
468 radius range that the initial DSD occupies. All the schemes converge as bin grids are refined.
469 Although the converged number concentrations obtained from the two advection schemes seem to
470 be slightly different from those obtained with the reassigning schemes or the reference experiment,
471 the difference is less than 1%. Interestingly, the 2MOM scheme underestimates the drop number
472 concentration but overestimates the drop mixing ratio at a relatively coarse bin grid, and the reverse
473 is true for the 3MOM scheme. Note that a kink in drop number concentrations obtained using the
474 dynamic grid is related to evaporation of cloud droplets. Cloud droplets that have completely
475 evaporated in some bin refinements may remain as very small cloud droplets in other bin

refinements. This depends largely on non-physical factors such as model integration period, time step length, etc., which are not regarded as very important.

Overall, the 3MOM, PPM, and the Bott schemes all yield reasonable solutions for evaporation with a geometric bin grid in which *s* is greater than or equal to two. When considering the shape of DSD, the two advection schemes are regarded as better for solving evaporation than the two reassigning schemes.

4. 3-D LES model

To examine the effects of numerical diffusion from solving condensation and evaporation in a more realistic framework, we conduct a series of numerical simulations for weakly drizzling stratocumulus. The Distributed Hydrodynamic Aerosol and Radiative Modeling Application (DHARMA) model (Ackerman et al. 2004, and references therein) is used as the LES model, coupled with the Community Aerosol-Radiative-Microphysics Application (CARMA, Ackerman et al. 1995; Jensen et al. 1998) bin microphysics model.

To evaluate spatial advection of scalars in the LES model, a third-order flux is calculated using a second-order forward-in-time method (Stevens and Bretherton 1996). The fluxes through cell faces are evaluated based on an upwind method but the highest-order term includes a centered difference. The PPM scheme is used to calculate the renormalization step in condensation and evaporation. Unlike the parcel or column model used above, the LES model conducts the renormalization computation every fast microphysical time step, which is applied to calculate the rate of change of drop mass from condensation and evaporation and can be as small as 0.1 s. To investigate the effects of numerical diffusion from solving condensation, we examine two types of bin grids. One is a geometric bin grid, which is widely used in bin microphysics models, with an

499 *s* value of 2 [referred as "S2" hereafter, see (3)], and the other is the mixed grid introduced above
500 with *d* and *s* values set to 4 and 2, respectively [referred as "M4", see (5)]. The number of bins in
501 the range $r < 25$ μm is 29 and 96 in the S2 and the M4 grids, respectively, and the total number of
502 bins to cover the maximum radius of 1 cm is 80 and 169 in the S2 and the M4 grids, respectively.
503 We include two improvements to the LES model compared with that used in Lee et al. (2019):
504 TICE are now included following Ayala et al. (2008) and Wang and Grabowski (2009), and the
505 sedimentation of drops is now always evaluated with the PPM scheme using substepping in time
506 where necessary to render it unconditionally stable (i.e., CFL number must be always less than or
507 equal to unity).

508 The initial thermodynamic and wind profiles are the same as in Rémillard et al. (2017) and
509 Lee et al. (2019), which represent a case of drizzling stratocumulus observed on 22 November
510 2009 during the Clouds, Aerosols, and Precipitation in the Marine Boundary Layer (CAP-MBL)
511 campaign (Wood et al. 2015). Rémillard et al. (2017) provides the detailed profiles of initial
512 conditions and hygroscopic aerosol specification. Aerosol consumption is neglected. The domain
513 size is 4.8 km × 4.8 km × 2.5 km. The horizontal grid spacing is constant at 75 m, and the vertical
514 grid spacing is varied between 10 and 20 m with finest at the surface and the boundary layer top.
515 Model integration is performed for 28 h. The dynamic model time step is adaptive in the range of
516 4–5 s.

517 Figure 14 shows the time series of some cloud quantities. While the two simulations share
518 the basic aspects of cloud development (e.g., closed cell structure, relatively low surface
519 precipitation rate, and increasing liquid water path (LWP) until $t < 20$ h), the largest drop radius is
520 always smaller by a few microns in the M4 simulation than in the S2 simulation. Surface
521 precipitation is visible a few hours later and is generally smaller in the M4 simulation. In the

precipitating stage (t > 22 h), the decrease in cloud drop number concentration is more evident in the S2 simulation. All these differences are consistent with the previous parcel and column model simulations. The bin grid refinement suppresses numerical diffusion from solving condensation, and this causes the decrease in the largest drop radius, delayed onset of surface precipitation, and the decreased surface precipitation in the LES results. However, the differences between the two simulations are not so large, consistent with the limitation of convergence in solving condensation during Eulerian vertical advection and collision-coalescence in the LES model, shown in the simplified model frameworks (Figs. 6 and 8). In addition, while the parcel model does not consider sedimentation and the large drops continuously grow by colliding with small drops, the simulations using the 3-D LES model consider sedimentation as well as the continuous nucleation, so the largest drop radius in the 3-D simulations does not exceed ~26 μm.

Figure 15 shows the Doppler radar spectra moments obtained from the two simulations and observations. Observations of backscattering radar cross sections are obtained from the W-band Atmospheric Radiation Measurement (ARM) cloud radar (WACR; Mead and Widener 2005) and used for comparison. The MRDSS forward simulator is employed to derive Doppler radar spectra and their moments from bin microphysics model output. Simulation results between t = 16 and 22 h are used to compare the simulations and observations. Similar to Lee et al. (2019), LWPs in a range between 140 and 240 g m^{-2}, which correspond to the one standard deviation below and above the mean LWP in the simulations, are used to filter the simulations and observations. The median values of spectral moments are picked at a given height and a radar reflectivity factor binned by 2-dBZ intervals. Radar spectra are averaged using a weighting function to match the vertical spacing of the LES model to that of the radar.

Compared to the S2 simulation, in the M4 simulations, the mean Doppler velocity is slightly decreased near the surface, which reflects decreased drizzle size (Fig. 14e), and becomes closer to observations. The width of Doppler spectra increases in clouds, and the increase is more distinct in high reflectivity regions. This increased Doppler spectral width with the finer bin spacing is also closer to observations. Doppler spectra are skewed more negatively (i.e., a longer large drop tail) in the relatively low reflectivity regions of clouds but more positively (i.e., a longer small drop tail) in the relatively high reflectivity regions. All these features are consistent with the results shown in the simplified model frameworks (Fig. 11), in which the spectral width increases and the spectral skewness shows a greater change as the bin grid is refined. However, it should be noted that the width and skewness of spectra in the sub-cloud layers still show clear deviations from observations. The simulations tend to yield wider and almost unskewed spectra, whereas observations show narrower and positively skewed spectra below the cloud base. There are several plausible reasons: for example, turbulence substantially affects width of radar spectra in the sub-cloud layers. More accurate descriptions for cloud microphysical processes, as well as more accurate numerics, are also crucial to demystify cloud development and drizzle formation using a bin microphysics model.

5. Summary and conclusions

In this study, we investigated convergence of condensation and evaporation solutions in a one-moment size-resolved ("bin") microphysics framework. As the renormalization step is responsible for numerical diffusion along the size axis in a bin microphysics model while solving condensation and evaporation, several numerical schemes are evaluated in solving the renormalization step on various bin grid refinements. Two of them are based on reassigning and

567 the others on Eulerian advection. In a parcel model framework, all of the examined schemes
568 converge to a reference solution obtained with a dynamically moving size bin grid that minimizes
569 numerical diffusion. The advection schemes are generally superior in yielding less numerical
570 diffusion than the reassigning schemes in solving condensation with a given bin grid. The width
571 of drop size distributions obtained using the bin microphysics model is largely restricted to a bin
572 grid width. Thus, a linear bin grid, in which bin widths are generally smaller than those in the
573 corresponding geometric grid, is more appropriate to solve condensation. The schemes were also
574 examined in solving evaporation with the same model framework. As in condensation, all the
575 schemes converge to a reference solution, even on a relatively coarse bin grid. The two advection
576 schemes are still better than the two reassigning schemes.

577 Morrison et al. (2018) recently pointed out that numerical diffusion from solving
578 condensation can be substantial if condensation is combined with Eulerian vertical advection and
579 continuous nucleation. This study revisited the numerical diffusion that was investigated in
580 Morrison et al. (2018). We found that convergence in solving condensation with respect to bin grid
581 refinement is limited to a certain extent by Eulerian vertical advection, as concluded by Morrison
582 et al. (2018). While the results of this study and Morrison et al. (2018) are generally consistent, we
583 also found that such a limitation appears at coarser bin grids as the number of iterations in vertical
584 advection increases. Thus, changing vertical grid spacing or dynamic model time step in a manner
585 that falls further below unity in Courant condition, as well as adopting a higher-order time
586 integration method, worsened numerical diffusion.

587 Drop size distribution broadening in condensation is particularly important when collision-
588 coalescence follows condensation. We explicitly examined the effects of numerical diffusion on
589 collision-coalescence using the parcel model framework. We introduced a mixed bin grid to take

advantage of a linear bin grid in solving condensation while still efficiently covering a wide range of drop radius. However, even a tiny difference in drop size distribution width (less than 0.5 μm) from condensation is shown to cause a distinct difference when condensation and collision-coalescence are combined. In addition to acceleration of drop size distribution evolution, moments of Doppler spectra as a function of radar reflectivity factor also exhibit distinct differences. However, if turbulence-induced collision enhancement, which accelerates collision of drops particularly with similar sizes, is implemented in the model, those differences substantially diminish. This implies that the effects of numerical broadening from solving condensation might not be so influential if turbulence effects, such as collision enhancement, spatial supersaturation fluctuation, or eddy hopping (e.g., Abade et al. 2018; Pardo et al. 2020), are well considered in a cloud model.

To examine the effects of numerical broadening from solving condensation in a more realistic framework, we conducted a few simulations using an LES model coupled with a bin microphysics model. Two types of bin grids, one a typical geometric grid and the other a mixture of linear and geometric grids, were employed in the model. While overall aspects of cloud development are unchanged, the simulation with the finer bin grid yields smaller large drop radius and later onset of surface precipitation, which is consistent with those obtained using the simplified model frameworks. Moments of the drop size distribution in radar reflectivity space are also changed in the directions expected. Those obtained using the finer bin grid are generally closer to observations, but the simulations remain more similar to one another than the observations overall. Of particular concern, the broadening introduced by solving condensation is likely presenting a limitation on convergence in both simulations. The broadening appears more clearly when it combines with collision-coalescence that amplifies even tiny drop size distribution broadening and

613 with vertical advection that is calculated with overly large vertical grid spacing or has Courant
614 numbers deviating from unity throughout the LES domain.

615 Explaining phenomena occurring in clouds using a numerical model is likely to contain
616 errors. Using bin microphysics schemes to study drizzle formation, special attention should be paid
617 to reducing numerical diffusion. In this study, along with the Part I of our study, the numerical
618 diffusion along the size axis in a bin microphysics model can be controlled to some degree over
619 well-defined conditions (e.g., a sufficiently small vertical grid spacing, a vertical advection scheme
620 that minimizes numerical diffusion, and range of Courant number when treating condensation and
621 advection). However, unless paying special attention to design a treatment both in dynamics and
622 in microphysics to minimize numerical diffusion, bin microphysics schemes are vulnerable to its
623 impacts on the representation of drizzle formation. The tradeoff between numerical accuracy and
624 computational expense is also one of the considerations; using more than several hundreds of bins
625 might not be practical at this time if the model is used in a 3-D cloud simulation. A Lagrangian
626 cloud model, which is free from numerical diffusion from condensation, would be a good
627 benchmark for improving bin microphysics models, although it requires extensive computational
628 resources at this time (e.g., Pinsky et al. 2008b; Shima et al. 2009). Observed cloud radar Doppler
629 spectra and a forward simulator, which can in principle produce Doppler spectra from any type of
630 model results under the assumption that it takes accurate account of physical phenomena such as
631 turbulent broadening of drop size distributions, are valuable tools for establishing that simulations
632 can reproduce observations and likely for the correct reasons. Continuing to simultaneously exploit
633 increasingly well-designed models and detailed observations can be expected to soundly increase
634 understanding of cloud and precipitation development.
635

Acknowledgements.

The authors thank Hugh Morrison and two anonymous reviewers for helpful comments. This work was supported by the Office of Science (BER), U.S. Department of Energy, under Agreement DE-SC0016237, and by the NASA Radiation Science Program. Resources supporting this work were provided by the NASA High-End Computing (HEC) Program through the NASA Advanced Supercomputing (NAS) Division at Ames Research Center. The first author was also supported by the National Research Foundation (NRF) of Korea grant funded by the Korea government (MSIT) (NRF-2020R1G1A1014637) and by the National Research Foundation (NRF) of Korea grant funded by the Korea government (MSIT) (NRF- 2019M1A2A2103954).

References

Abade, G. C., W. W. Grabowski, and H. Pawlowska, 2018: Broadening of cloud droplet spectra through eddy hopping: Turbulent entraining parcel simulations. *J. Atmos. Sci.*, **75**, 3365–3378, doi:10.1175/JAS-D-18-0078.1.

Ackerman, A. S., O. B. Toon, and P. V. Hobbs, 1995: A model for particle microphysics, turbulent mixing, and radiative transfer in the stratocumulus-topped marine boundary layer and comparisons with measurements. *J. Atmos. Sci.*, **52**, 1204–1236, doi:10.1175/1520-0469(1995)052<1204:AMFPMT.2.0>CO;2.

Ackerman, A. S., M. P. Kirkpatrick, D. E. Stevens, and O. B. Toon, 2004: The impact of humidity above stratiform clouds on indirect aerosol climate forcing. *Nature*, **432**, 1014–1017, doi:10.1038/nature03174.

Ayala, O., B. Rosa, and L.-P. Wang, 2008: Effects of turbulence on the geometric collision rate of sedimenting droplets. Part 2. Theory and parameterization. *New J. Phys.*, **10**, 075016, doi:10.1088/1367-2630/10/7/075016.

Beard, K. V., 1976: Terminal velocity and shape of cloud and precipitation drops aloft. *J. Atmos. Sci.*, **33**, 851–864, doi:10.1175/1520-0469(1976)033<0851:TVASOC>2.0.CO;2.

Berry, E. X., and R. L. Reinhardt, 1974: An analysis of cloud drop growth by collection: Part I. Double distributions. *J. Atmos. Sci.*, **31**, 1814–1824, doi:10.1175/1520-0469(1974)031<1814:AAOCDG>2.0.CO;2.

Bott, 1989: A positive definite advection scheme obtained by nonlinear renormalization of the advective fluxes. *Mon. Wea. Rev.*, **117**, 1006–1015, doi:10.1175/1520-0493(1989)117<1006:APDASO>2.0.CO;2.

668 Bott, 2000: A flux method for the numerical solution of the stochastic collection equation:
669 Extension to two-dimensional particle distributions. *J. Atmos. Sci.*, **57**, 284–294,
670 doi:10.1175/1520-0469(2000)057<0284:AFMFTN>2.0.CO;2.
671 Colella, P., and P. R. Woodward, 1984: The Piecewise Parabolic Method (PPM) for gas-
672 dynamical simulations. *J. Comput. Phys.*, **54**, 174–201, doi:10.1016/0021-
673 9991(84)90143-8.
674 Cooper, W. A., R. T. Bruintjes, and G. K. Mather, 1997: Calculations pertaining to hygroscopic
675 seeding with flares. *J. Appl. Meteor.*, **36**, 1449–1469, doi:10.1175/1520-
676 0450(1997)036<1449:CPTHSW>2.0.CO;2.
677 Grabowski, W. W., M. Andrejczuk, and L.-P. Wang, 2011: Droplet growth in a bin warm-rain
678 scheme with Twomey CCN activation. *Atmos. Res.*, **99**, 290–301,
679 doi:10.1016/j.atmosres.2010.10.020.
680 Egan, B. A., and J. R. Mahoney, 1972: Numerical modeling of advection and diffusion of urban
681 area source pollutants. *J. Appl. Meteor.*, **11**, 312–322, doi:10.1175/1520-
682 0450(1972)011<0312:NMOAAD>2.0.CO;2.
683 Franklin, C. N., 2008: A warm rain microphysics parameterization that includes the effect of
684 turbulence. *J. Atmos. Sci.*, **65**, 1795–1816, doi:10.1175/2007JAS2556.1.
685 Hall, W. D., 1980: A detailed microphysics model within a two-dimensional dynamic
686 framework: Model description and preliminary results. *J. Atmos. Sci.*, **37**, 2486–2507,
687 doi:10.1175/1520-0469(1980)037<2486:ADMMWA>2.0.CO;2.
688 Jensen, E. J., and Coauthors, 1998: Ice nucleation processes in upper tropospheric wave-clouds
689 observed during SUCCESS. *Geophys. Res. Lett.*, **25**, 1363–1366,
690 doi:10.1029/98GL00299.

691 Khain, A., and I. Sednev, 1996: Simulation of precipitation formation in the Eastern
692 Mediterranean coastal zone using a spectral microphysics cloud ensemble model. *Atmos.*
693 *Res.*, **43**, 77–110, doi:10.1016/S0169-8095(96)00005-1.
694 Khain, A., M. Ovtchinnikov, M. Pinsky, A. Pokrovsky, and H. Krugliak, 2000: Notes on the
695 state-of-the-art numerical modeling of cloud microphysics. *Atmos. Res.*, **55**, 159–224,
696 doi:10.1016/S0169-8095(00)00064-8.
697 Khain, A., N. Benmoshe, and A. Pokrovsky, 2008: Factors determining the impact of aerosols on
698 surface precipitation from clouds: An attempt at classification. *J. Atmos. Sci.*, **65**, 1721–
699 1748, doi:10.1175/2007JAS2515.1.
700 Khain, A., and Coauthors, 2015: Representation of microphysical processes in cloud-resolving
701 models: Spectral (bin) microphysics versus bulk parameterization. *Rev. Geophys.*, **53**,
702 247–322, doi:10.1002/2014RG000468.
703 Khairoutdinov, M., and Y. Kogan, 2000: A new cloud physics parameterization in a large-eddy
704 simulation model of marine stratocumulus. *Mon. Wea. Rev.*, **128**, 229–243,
705 doi:10.1175/1520-0493(2000)128<0229:ANCPPI>2.0.CO;2.
706 Kollias, P., S. Tanelli, A. Battaglia, and A. Tatarevic, 2014: Evaluation of EarthCARE cloud
707 profiling radar Doppler velocity measurements in particle sedimentation regimes. *J.*
708 *Atmos. Oceanic Technol.*, **31**, 366–386, doi:10.1175/JTECH-D-11-00202.1.
709 Kovetz, A., and B. Olund, 1969: The effect of coalescence and condensation on rain formation in
710 a cloud of finite vertical extent. *J. Atmos. Sci.*, **26**, 1060–1065, doi:10.1175/ 1520-
711 0469(1969)026<1060:TEOCAC>2.0.CO;2.
712 Lee, H., and J.-J. Baik, 2017: A physically based autoconversion parameterization. *J. Atmos.*
713 *Sci.*, **74**, 1599–1616, doi:10.1175/JAS-D-16-0207.1.

Lee, H., J.-J. Baik, and J.-Y. Han, 2015: Effects of turbulence on warm clouds and precipitation with various aerosol concentrations. *Atmos. Res.*, **153**, 19–33, doi:10.1016/j.atmosres.2014.07.026.

Lee, H., A. M. Fridlind, and A. S. Ackerman, 2019: An evaluation of size-resolved cloud microphysics scheme numerics for use with radar observations. Part I: Collision–coalescence. *J. Atmos. Sci.*, **76**, 247–263, doi:10.1175/JAS-D-18-0174.1.

Liu, Q., Y. L. Kogan, D. K. Lilly, and M. P. Khairoutdinov, 1997: Variational optimization method for calculation of cloud drop growth in an Eulerian drop-size framework. *J. Atmos. Sci.*, **54**, 2493–2504, doi:10.1175/1520-0469(1997)054<2493:VOMFCO>2.0.CO;2.

Mead, J. B., and K. B. Widener, 2005: W-band ARM cloud radar. *32nd Int. Conf. on Radar Meteorology*, Albuquerque, NM, Amer. Meteor. Soc., P1R.3, https://ams.confex.com/ams/pdfpapers/95978.pdf.

Morrison, H., M. Witte, G. H. Bryan, J. Y. Harrington, and Z. J. Lebo, 2018: Broadening of modeled cloud droplet spectra using bin microphysics in an Eulerian spatial domain. *J. Atmos. Sci.*, **75**, 4005–4030, doi:10.1175/JAS-D-18-0055.1.

Pardo, L. H., H. Morrison. L. A. T. Machado, J. Y. Harrington, and Z. J. Lebo, 2020: Drop size distribution broadening mechanisms in a bin microphysics Eulerian model. *J. Atmos. Sci.*, **77**, 3249–3273.

Pinsky, M., A. Khain, and H. Krugliak, 2008a: Collisions of cloud droplets in a turbulent flow. Part V: Application of detailed tables of turbulent collision rate enhancement to simulation of droplet spectra evolution. *J. Atmos. Sci.*, **65**, 357–374, doi:10.1175/2007JAS2358.1.

737 Pinsky, M., L. Magaritz, A. Khain, O. Krasnov, and A. Sterkin, 2008b: Investigation of droplet
738 size distributions and drizzle formation using a new trajectory ensemble model. Part I:
739 Model description and first results in a nonmixing limit. *J. Atmos. Sci.*, **65**, 2064–2086,
740 doi:10.1175/2007JAS2486.1.
741 Pruppacher, H. R., and J. D. Klett, 1997: *Microphysics of Clouds and Precipitation*. Kluwer
742 Academic Publishers, 954 pp.
743 Rémillard, J., and Coauthors, 2017: Use of cloud radar Doppler spectra to evaluate stratocumulus
744 drizzle size distributions in large-eddy simulations with size-resolved microphysics. *J.*
745 *Appl. Meteor. Climatol.*, **56**, 3263–3283, doi:10.1175/JAMC-D-17-0100.1.
746 Rogers, R. R., and M. K. Yau, 1989: *A Short Course in Cloud Physics*. Butterworth Heinemann,
747 290 pp.
748 Seeßelberg, M., T. Trautmann, and M. Thorn, 1996: Stochastic simulations as a benchmark for
749 mathematical methods solving the coalescence equation. *Atmos. Res.*, **40**, 33–48,
750 doi:10.1016/0169-8095(95)00024-0.
751 Seifert, A., and K. D. Beheng, 2001: A double-moment parameterization for simulating
752 autoconversion, accretion and selfcollection. *Atmos. Res.*, **59–60**, 265–281,
753 doi:10.1016/S0169-8095(01)00126-0.
754 Seifert, A., L. Nuijens, and B. Stevens, 2010: Turbulence effects on warm-rain autoconversion in
755 precipitating shallow convection. *Quart. J. Roy. Meteor. Soc.*, **136**, 1753–1762,
756 doi:10.1002/qj.684.
757 Shima, S., K. Kusano, A. Kawano, T. Sugiyama, and S. Kawahara, 2009: The super-droplet
758 method for the numerical simulation of clouds and precipitation: A particle-based and

probabilistic microphysics model coupled with a non-hydrostatic model. *Quart. J. Roy. Meteor. Soc.*, **135**, 1307–1320, doi: 10.1002/qj.441.

Smolarkiewicz, P. K., 2006: Multidimensional positive definite advection transport algorithm: An overview. *Int. J. Numer. Meth. Fluids*, **50**, 1123–1144, doi:10.1002/fld.1071.

Stevens, D. E., and S. Bretherton, 1996: A forward-in-time advection scheme and adaptive multilevel flow solver for nearly incompressible atmospheric flow. *J. Comput. Phys.*, **129**, 284–295, doi:10.1006/jcph.1996.0250.

Wang, L.-P., and W. W. Grabowski, 2009: The role of air turbulence in warm rain initiation. *Atmos. Sci. Lett.*, **10**, 1–8, doi:10.1002/asl.210.

Wang, L.-P., Y. Xue, and W. W. Grabowski, 2007: A bin integral method for solving the kinetic collection equation. *J. Comput. Phys.*, **226**, 59–88, doi:10.1016/j.jcp.2007.03.029.

Wicker, L. J., and W. C. Skamarock, 2002: Time-splitting methods for elastic models using forward time schemes. *Mon. Wea. Rev.*, **130**, 2088–2097, doi:10.1175/1520-0493(2002)130<2088:TSMFEM>2.0.CO;2.

Witte, M. K., P. Y. Chuang, O. Ayala, L.-P., Wang, and G. Feingold, 2019: Comparison of observed and simulated drop size distributions from large-eddy simulations with bin microphysics. *Mon. Wea. Rev.*, **147**, 477–493, doi:10.1175/MWR-D-18-0242.1.

Wood, R., and Coauthors, 2015: Clouds, aerosols, and precipitation in the marine boundary layer: An ARM mobile facility deployment. *Bull. Amer. Meteor. Soc.*, **96**, 419–440, doi:10.1175/BAMS-D-13-00180.1.

Wyszogrodzki. A. A., W. W. Grabowski, L.-P. Wang, and O. Ayala, 2013: Turbulent collision-coalescence in maritime shallow convection. *Atmos. Chem. Phys.*, **13**, 8471–8487, doi:10.5194/acp-13-8471-2013.

782

List of Figures

Fig. 1. Size distributions of (a) number concentration, (b) mass concentration, and (c) Rayleigh-regime radar reflectivity factor of drops at t = 10 min obtained in the condensation experiments using different renormalization schemes, and the dynamic bin grid without any renormalization scheme. (d) As in (c), but as a function of drop fall speed.

Fig. 2. Time series of (a) the median radius, (b) the largest (99th percentile) radius, (c) difference in radius between the largest and the median, and (d) standard deviation of drop size distributions obtained using different renormalization schemes and a geometric grid, and the dynamic bin grid without any renormalization scheme. In the geometric grid, the bin width parameter s is set to 2.

Fig. 3. As in Fig. 2, but with a linear bin grid with the bin width parameter d of 1.

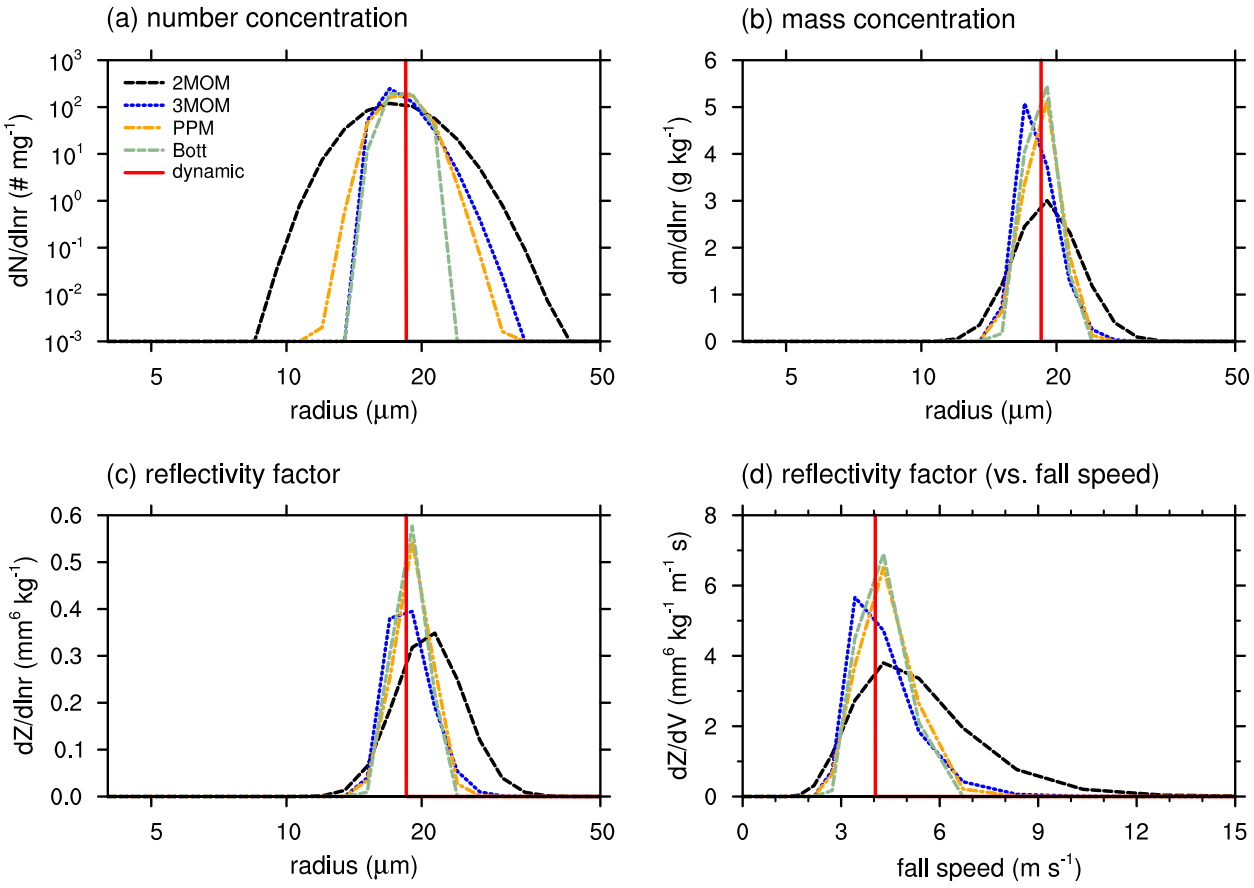
Fig. 4. (a) The largest radii and (b) standard deviations of drop size distributions as a function of bin width parameter. Solid lines represent results obtained using linear bin grids with varied parameter d, and dashed lines those with corresponding geometric bin grids with varied parameter s.

Fig. 5. (a)–(d) As in Fig. 3 but obtained using a column model and as a function of height. (e)–(h) As in (a)–(d) but obtained using the PPM renormalization scheme with varied bin width parameters.

Fig. 6. Standard deviations of drop size distributions as a function of bin width parameter d. The black solid line represents the result obtained using a third-order Runge-Kutta in time scheme, and the others using a first-order forward-in-time scheme. The red solid line represents the result obtained using the parcel model, and the others using the column

805 model. Two different vertical grid spacings (20 and 10 m) and two different time steps (5
806 and 1 s) are examined in the column model.
807 Fig.7. Radius bin grid spacing as a function of particle radius in a mixture grid with d = 4 and s =
808 2 (solid). It is readily seen that the grid spacing in the mixture grid is asymptotically
809 approaches that of a geometric grid with s = 2 (dashed) and is smaller in the radius range
810 of 5 – 40 μm than that of a geometric grid that covers the same radius range with the same
811 number of bins as the mixture grid (dotted).
812 Fig. 8. Time evolutions of size distributions of (top) number, (middle) mass, and (bottom) radar
813 reflectivity factor of drops. The PPM scheme is used to solve the renormalization step. The
814 first three columns are obtained using the mixture bin grid in which the bin width parameter
815 s is fixed at 2 and d is varied with (first column) 1, (second column) 4, and (third column)
816 16. The rightmost column is obtained using the dynamic bin grid.
817 Fig. 9. Time series of (a) radar reflectivity factor, (b) mean Doppler velocity, (c) width of Doppler
818 spectra, and (d) skewness of Doppler spectra obtained using the mixture bin grids with bin
819 width parameter d varied with 1, 4, and 16, and the dynamic bin grid.
820 Fig. 10. (a) Mean Doppler velocity, (b) width of Doppler spectra, and (c) skewness of Doppler
821 spectra as a function of radar reflectivity factor obtained using the mixture bin grids with
822 bin width parameter d varied with 1, 4, and 16, and the dynamic bin grid.
823 Fig. 11. As in Fig. 10, but for the parcel model that considers the turbulence-induced collision
824 enhancement.
825 Fig. 12. Size distributions of (a) number concentration, (b) mass concentration, and (c) Rayleigh-
826 regime radar reflectivity factor of drops at t = 20 min obtained in the evaporation

827 experiments using different renormalization schemes, and the dynamic bin grid without
828 any renormalization scheme. (d) As in (c), but as a function of drop fall speed.
829 Fig. 13. (a) Number concentration and (b) mass concentration of drops as a function of bin width
830 parameter *s*. Note that the lines obtained using the PPM and Bott schemes are almost
831 coincident.
832 Fig. 14. Time series of simulated domain-averaged (a) liquid water path, (b) cloud fraction, (c)
833 cloud drop number concentration, (d) surface precipitation rate, and (e) the largest drop
834 radius in the S2 and M4 simulations.
835 Fig. 15. Median of (top) mean Doppler velocity, (middle) width of Doppler spectra, and (bottom)
836 skewness of Doppler spectra for a given radar reflectivity factor range and height obtained
837 from (left) the S2 simulation, (center) the M4 simulation, and (right) observations. The sign
838 convention for Doppler velocities is negative for downward motion. Black horizontal lines
839 in the panels indicate the mean cloud-base heights.
840



841

842 Fig. 1. Size distributions of (a) number concentration, (b) mass concentration, and (c) Rayleigh-
843 regime radar reflectivity factor of drops at t = 10 min obtained in the condensation experiments
844 using different renormalization schemes, and the dynamic bin grid without any renormalization
845 scheme. (d) As in (c), but as a function of drop fall speed.

846

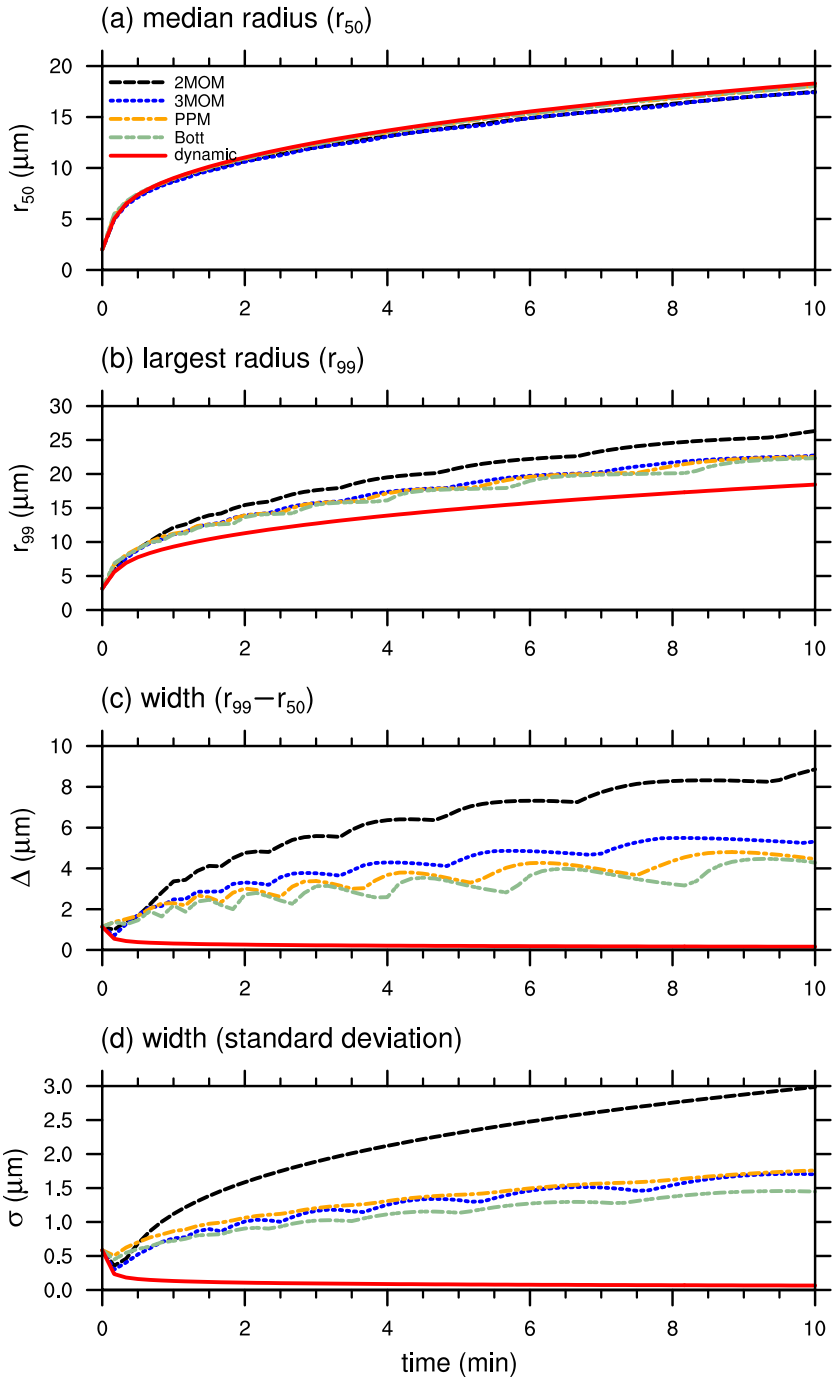
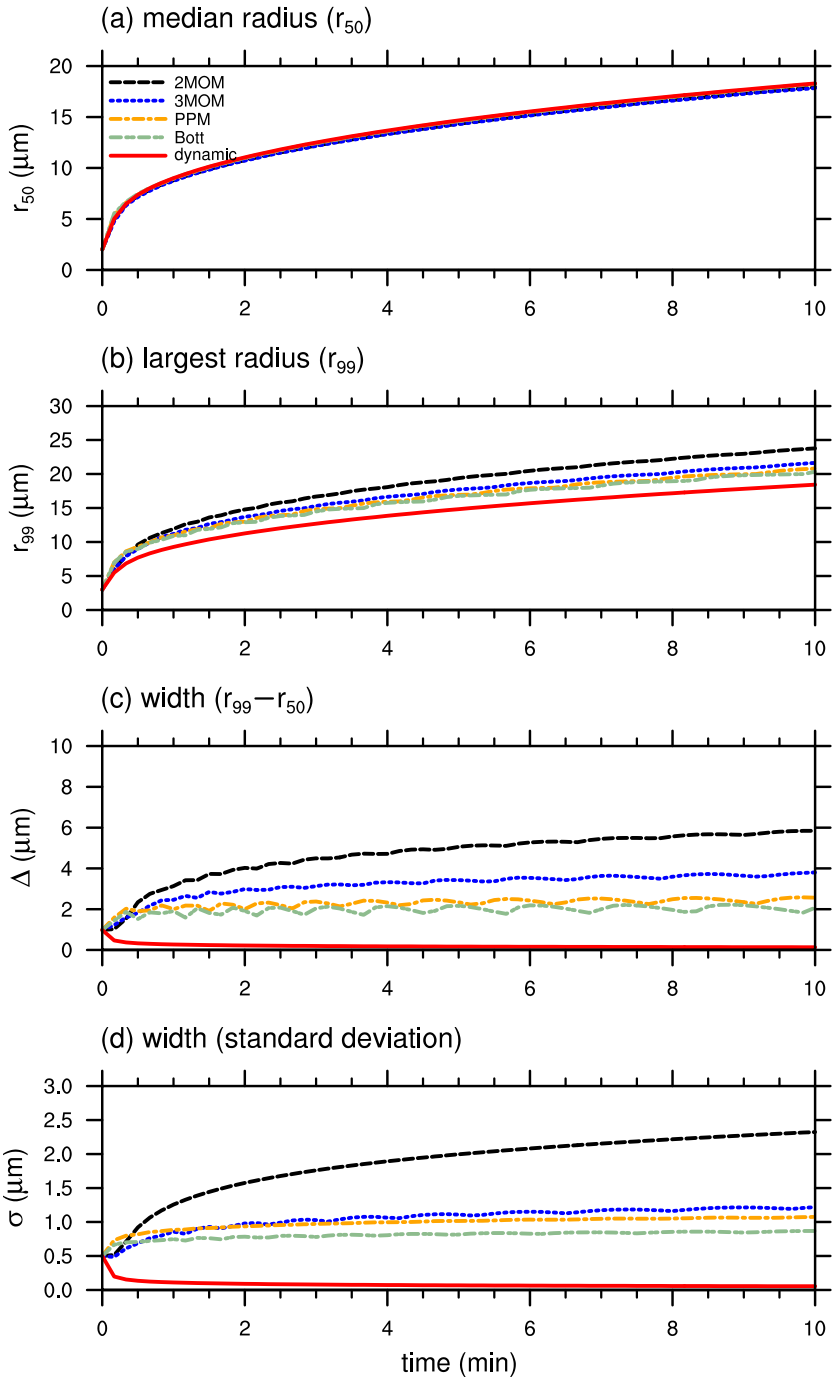


Fig. 2. Time series of (a) the median radius, (b) the largest (99th percentile) radius, (c) difference in radius between the largest and the median, and (d) standard deviation of drop size distributions obtained using different renormalization schemes and a geometric grid, and the dynamic bin grid without any renormalization scheme. In the geometric grid, the bin width parameter *s* is set to 2.



852

853 Fig. 3. As in Fig. 2, but with a linear bin grid with the bin width parameter *d* of 1.

854

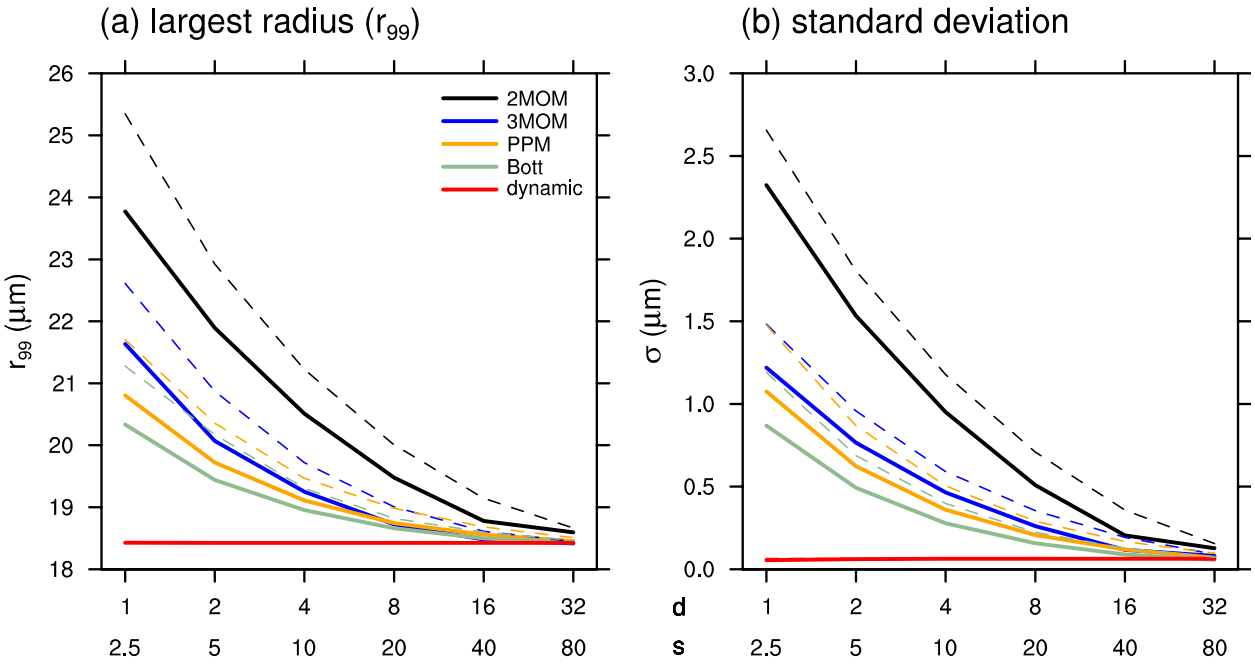


Fig. 4. (a) The largest radii and (b) standard deviations of drop size distributions as a function of bin width parameter. Solid lines represent results obtained using linear bin grids with varied parameter *d*, and dashed lines those with corresponding geometric bin grids with varied parameter *s*.

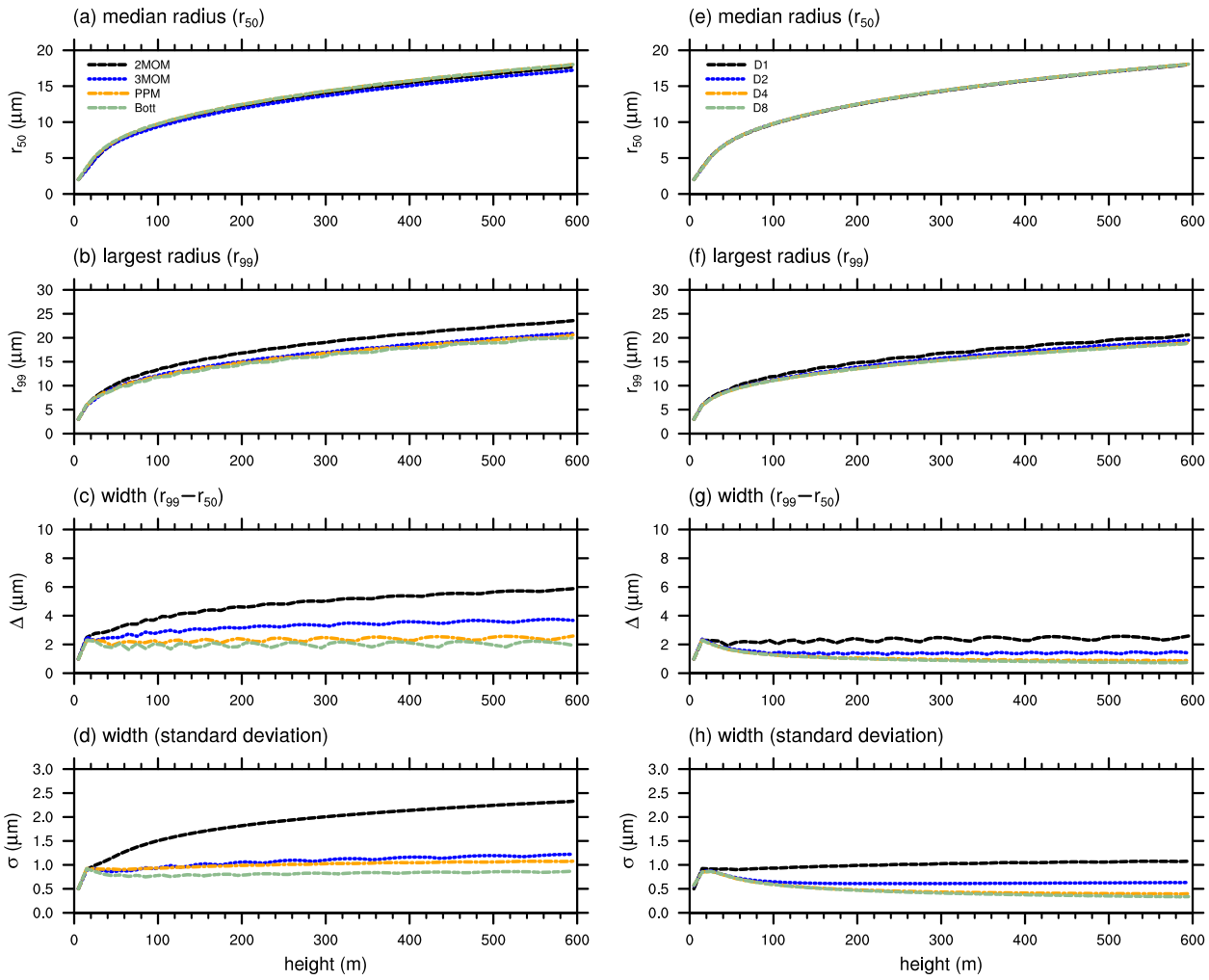


Fig. 5. (a)–(d) As in Fig. 3 but obtained using a column model and as a function of height. (e)–(h) As in (a)–(d) but obtained using the PPM renormalization scheme with varied bin width parameter *d*.

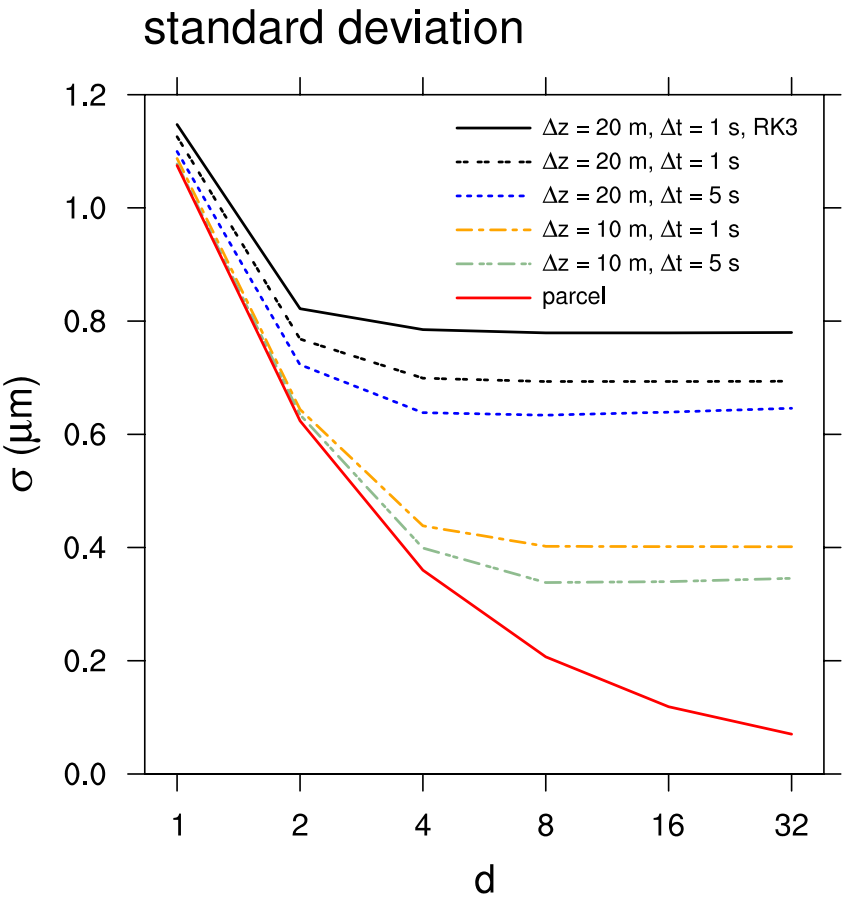
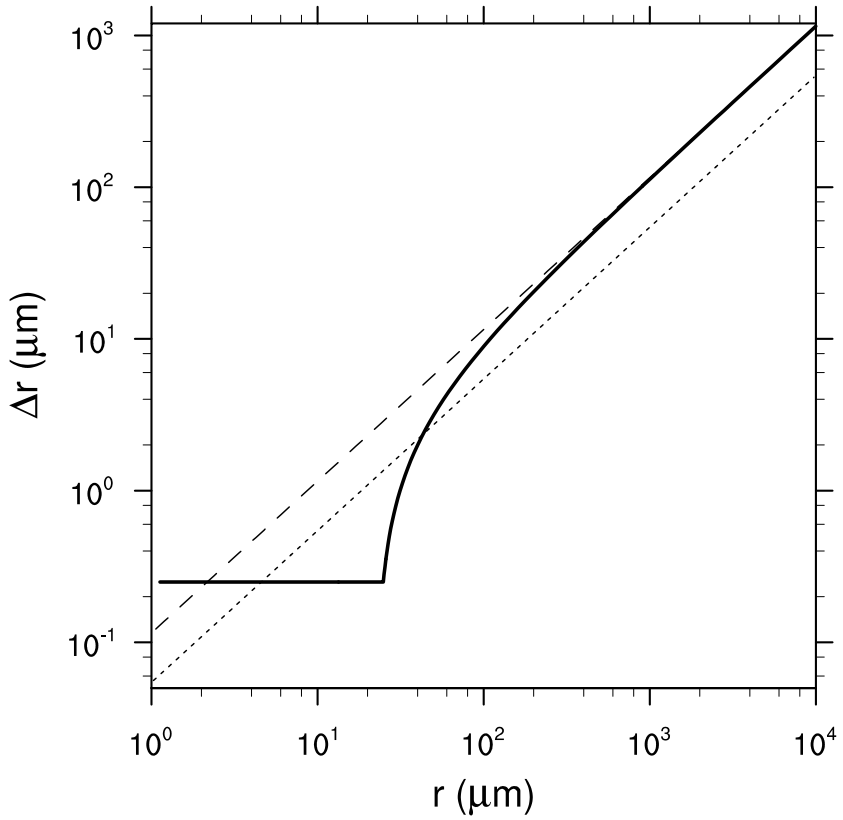


Fig. 6. Standard deviations of drop size distributions as a function of bin width parameter *d*. The black solid line represents the result obtained using a third-order Runge-Kutta in time scheme, and the others using a first-order forward-in-time scheme. The red solid line represents the result obtained using the parcel model, and the others using the column model. Two different vertical grid spacings (20 and 10 m) and two different time steps (5 and 1 s) are examined in the column model.



874

875 Fig.7. Radius bin grid spacing as a function of particle radius in a mixture grid with d = 4 and s =
876 2 (solid). It is readily seen that the grid spacing in the mixture grid is asymptotically approaches
877 that of a geometric grid with s = 2 (dashed) and is smaller in the radius range of 5 – 40 μm than
878 that of a geometric grid that covers the same radius range with the same number of bins as the
879 mixture grid (dotted).

880

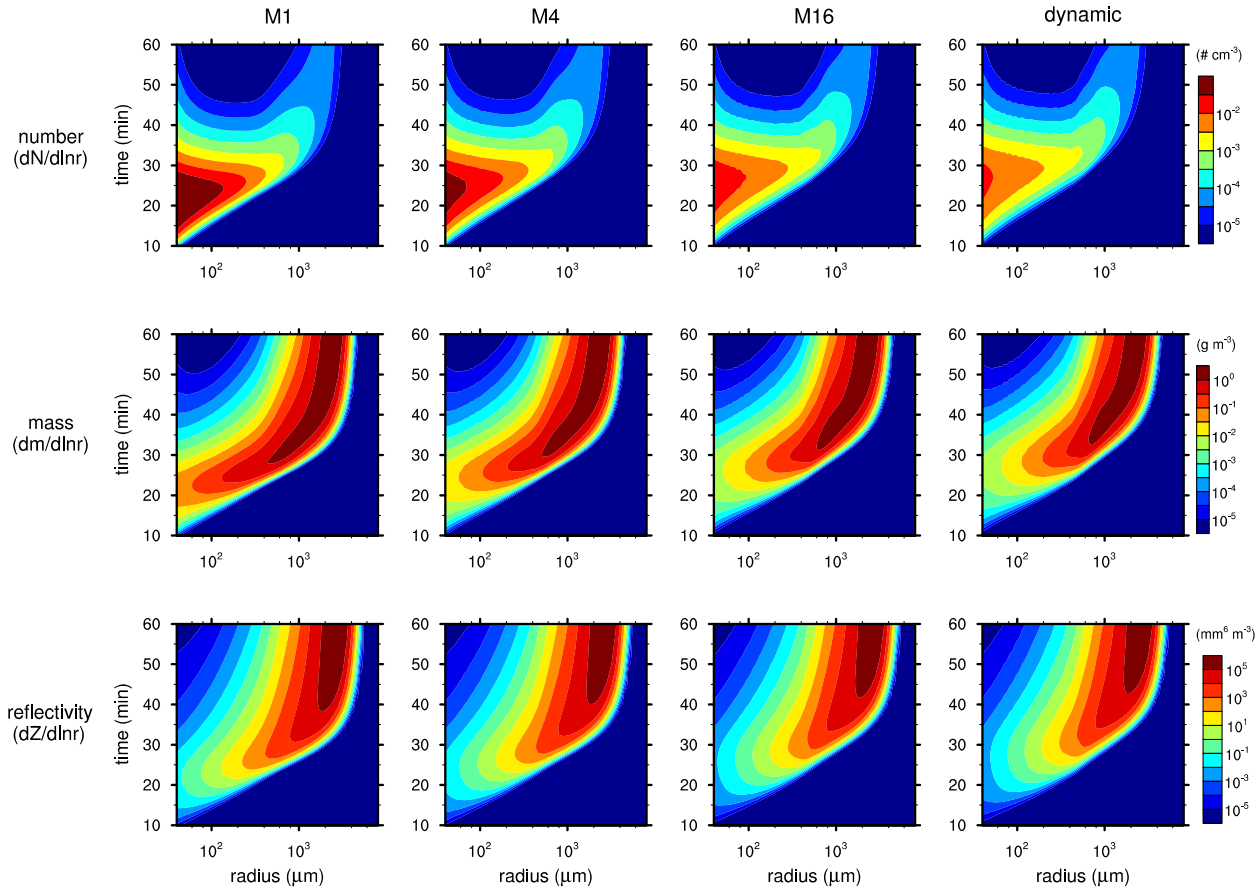
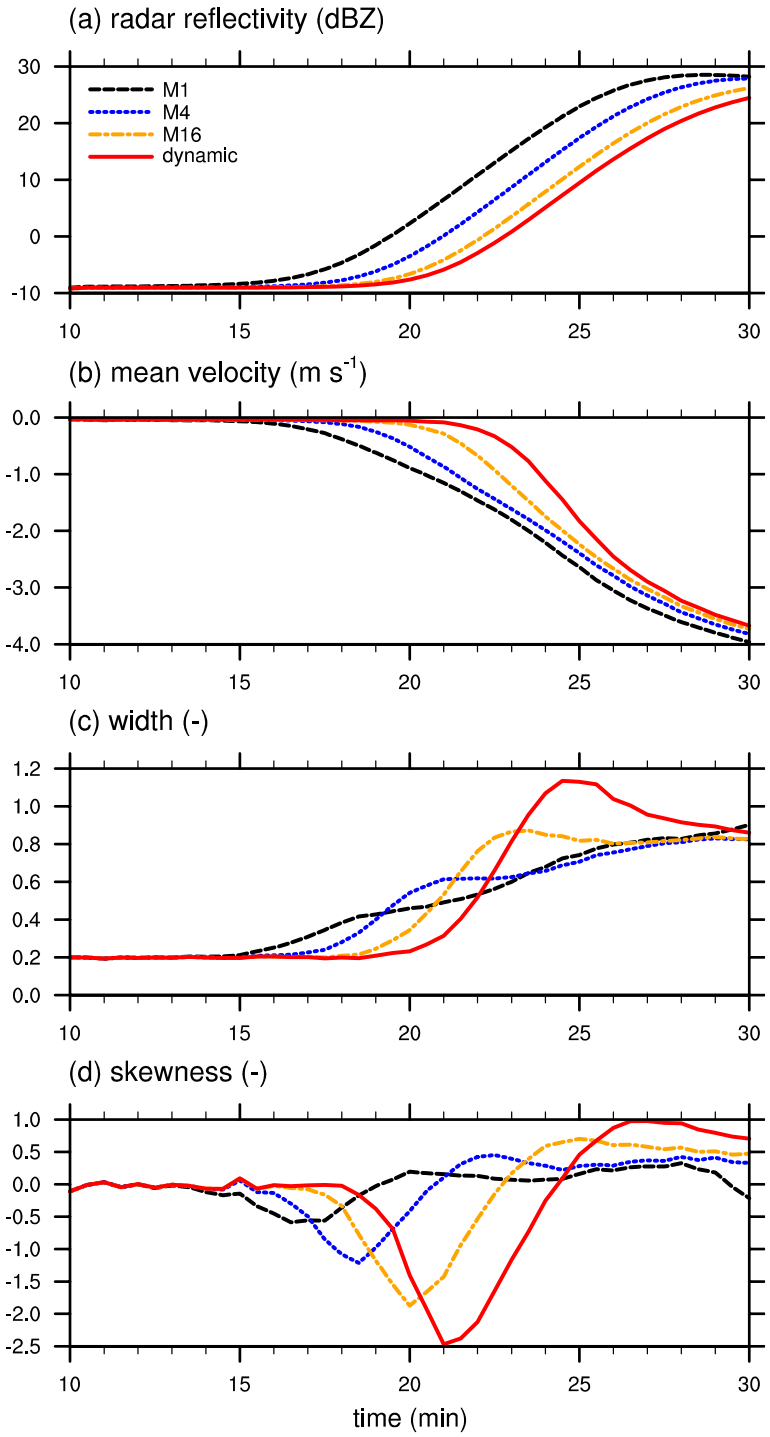


Fig. 8. Time evolutions of size distributions of (top) number, (middle) mass, and (bottom) radar reflectivity factor of drops. The PPM scheme is used to solve the renormalization step. The first three columns are obtained using the mixture bin grid in which the bin width parameter *s* is fixed at 2 and *d* is varied with (first column) 1, (second column) 4, and (third column) 16. The rightmost column is obtained using the dynamic bin grid.



888

889 Fig. 9. Time series of (a) radar reflectivity factor, (b) mean Doppler velocity, (c) width of Doppler

890 spectra, and (d) skewness of Doppler spectra obtained using the mixture bin grids with bin width

891 parameter *d* varied with 1, 4, and 16, and the dynamic bin grid.

892

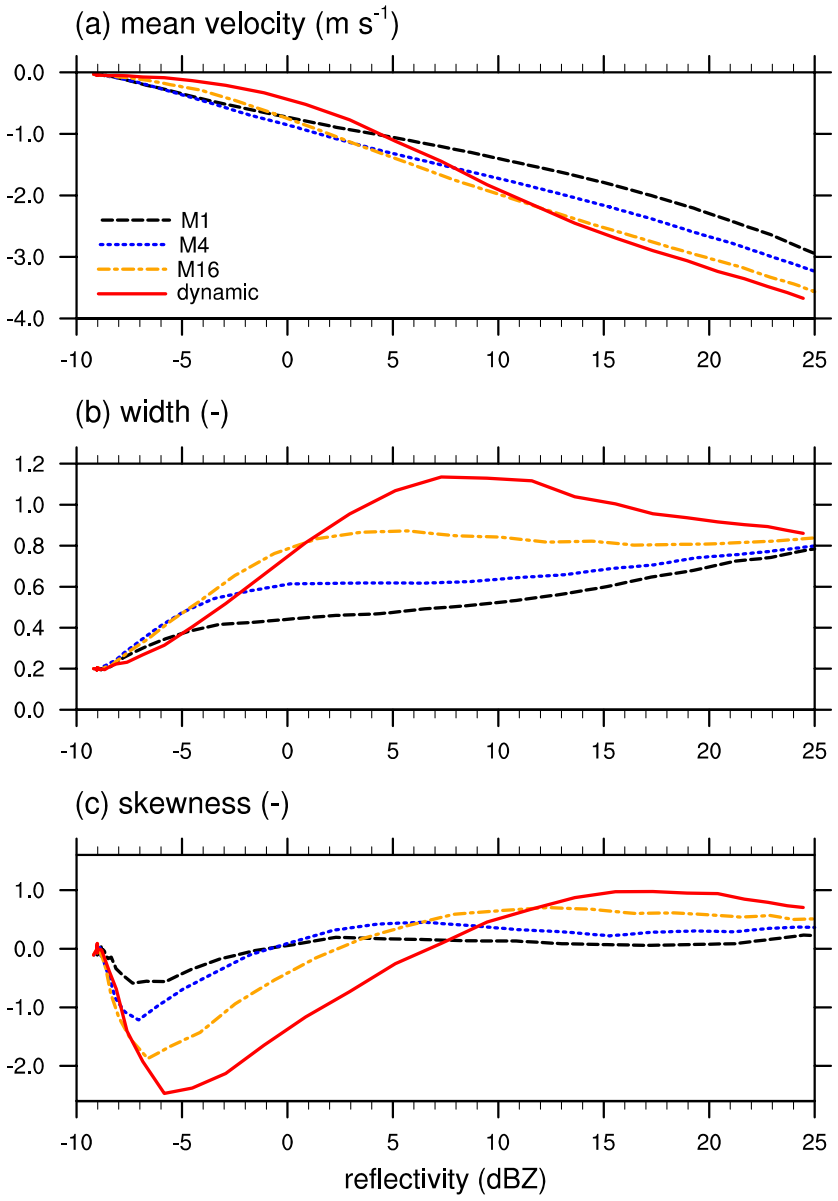
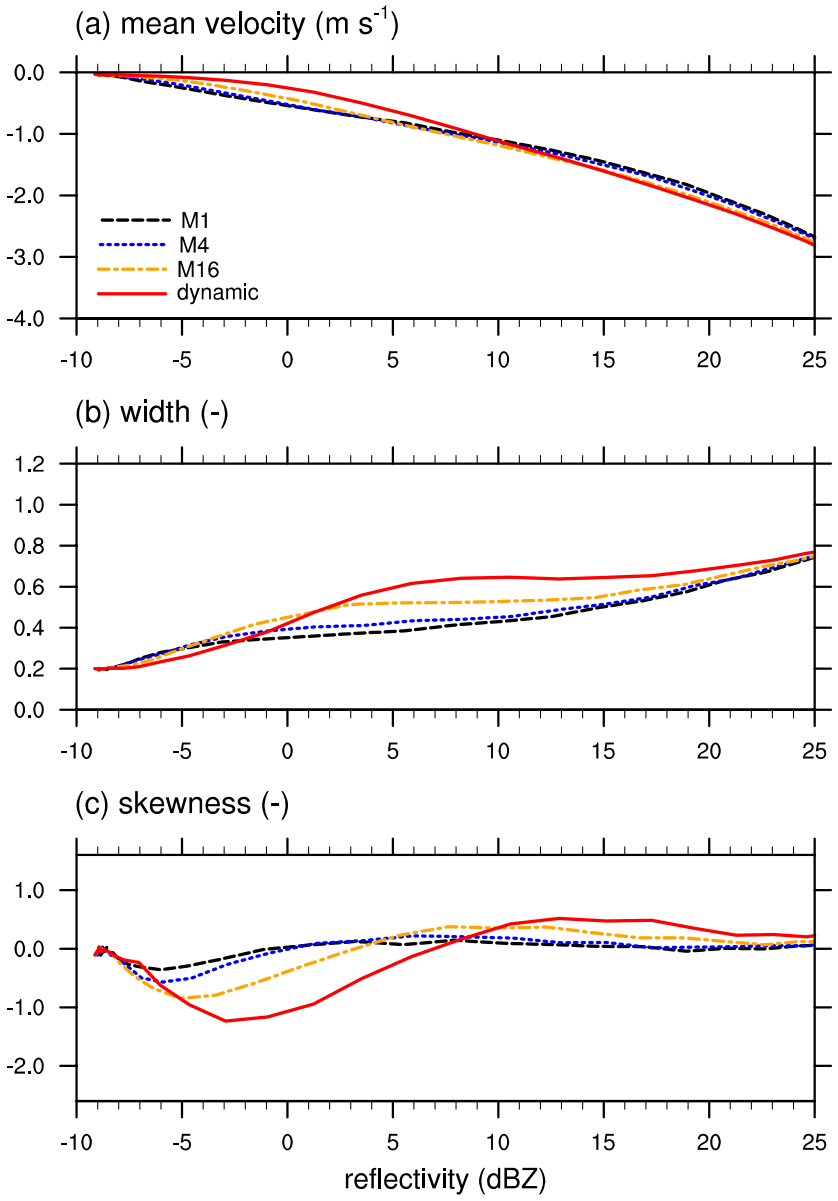


Fig. 10. (a) Mean Doppler velocity, (b) width of Doppler spectra, and (c) skewness of Doppler spectra as a function of radar reflectivity factor obtained using the mixture bin grids with bin width parameter *d* varied with 1, 4, and 16, and the dynamic bin grid.

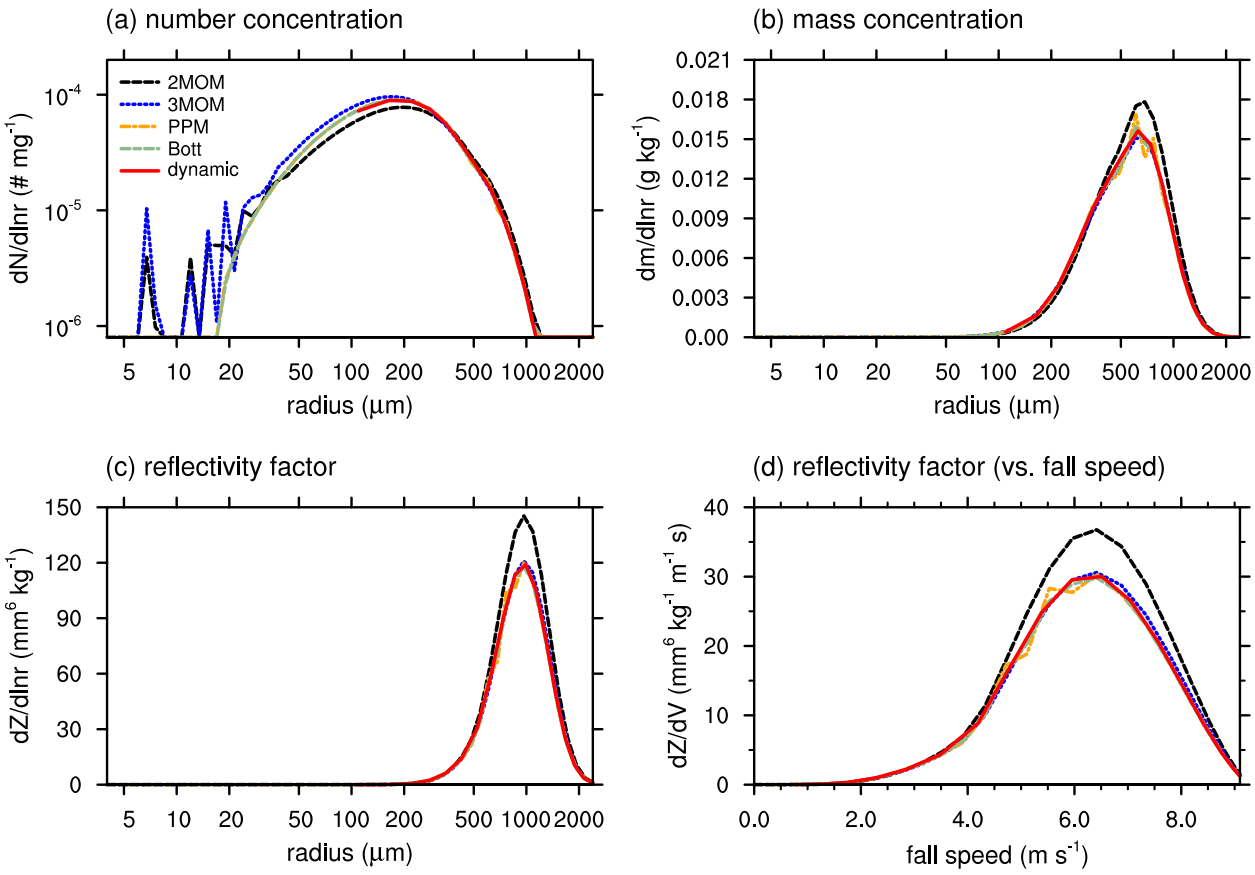


898

899 Fig. 11. As in Fig. 10, but for the parcel model that considers the turbulence-induced collision

900 enhancement.

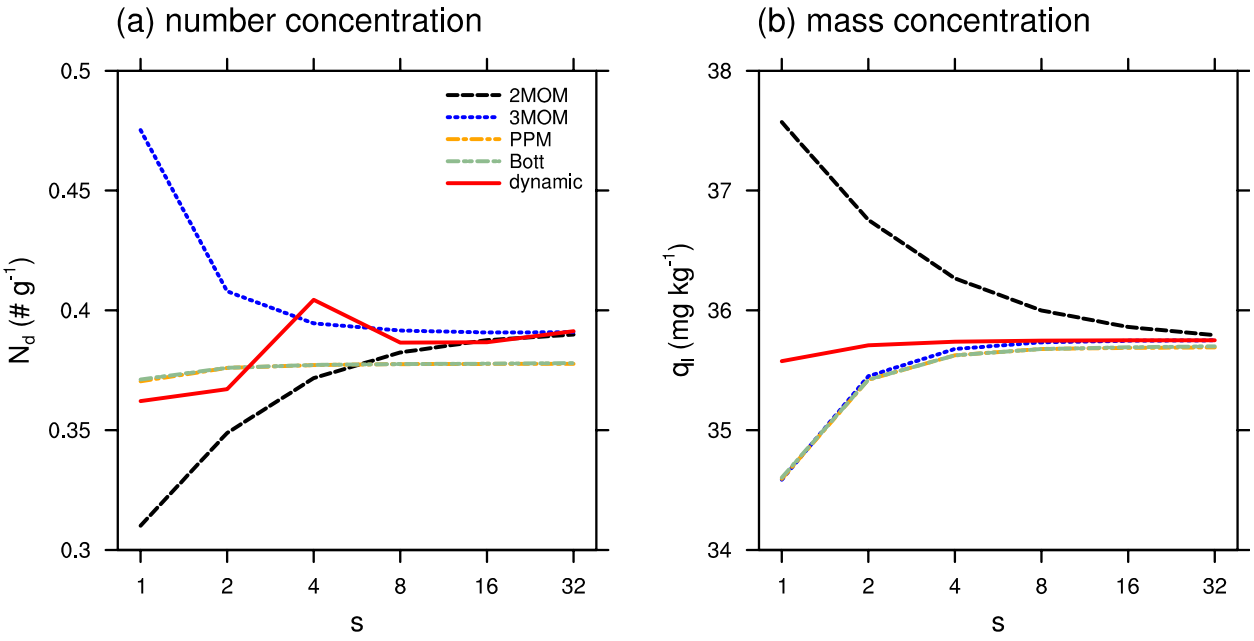
901



902

903 Fig. 12. Size distributions of (a) number concentration, (b) mass concentration, and (c) Rayleigh-
904 regime radar reflectivity factor of drops at t = 20 min obtained in the evaporation experiments
905 using different renormalization schemes, and the dynamic bin grid without any renormalization
906 scheme. (d) As in (c), but as a function of drop fall speed.

907

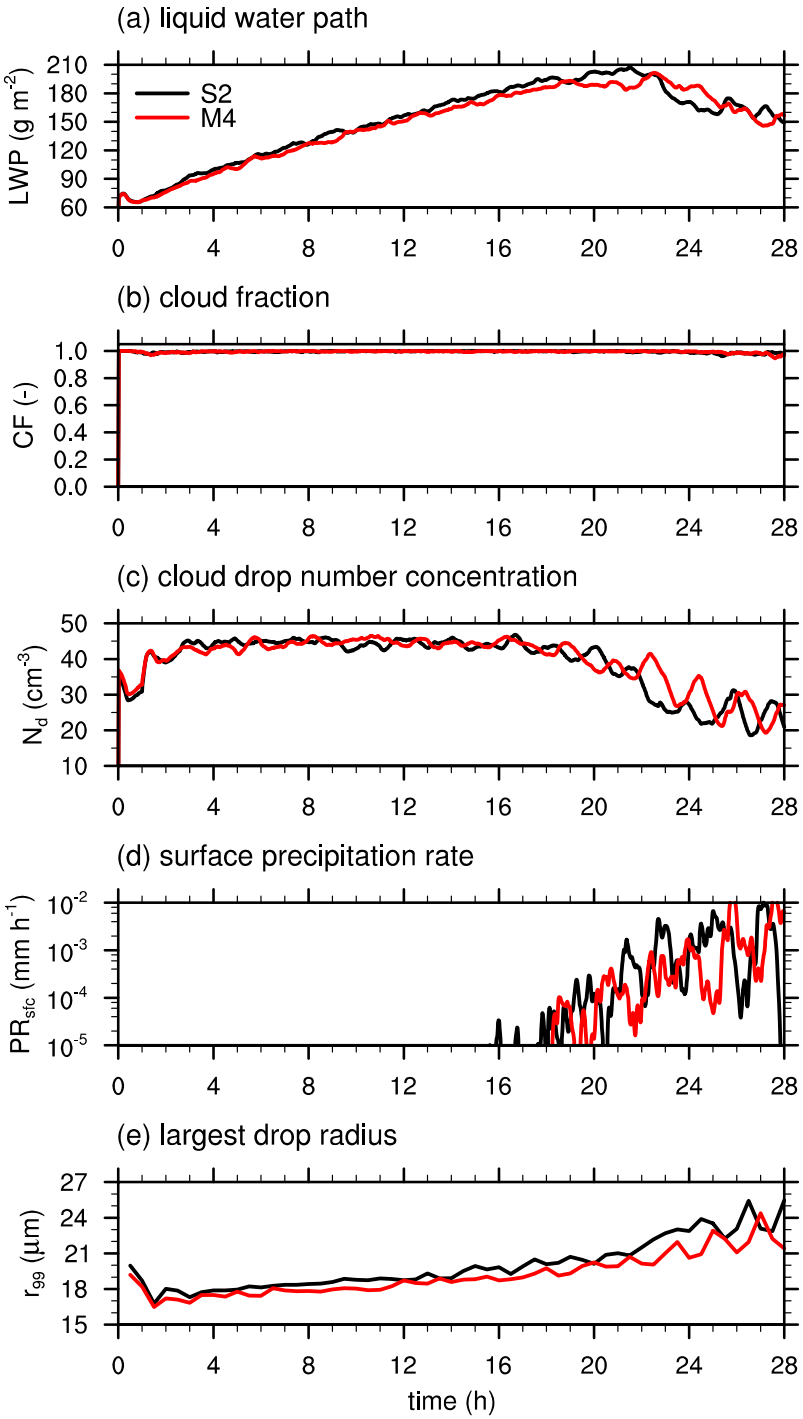


908

909 Fig. 13. (a) Number concentration and (b) mass concentration of drops as a function of bin width

910 parameter *s*. Note that the lines obtained using the PPM and Bott schemes are almost coincident.

911



912

913 Fig. 14. Time series of simulated domain-averaged (a) liquid water path, (b) cloud fraction, (c)

914 cloud drop number concentration, (d) surface precipitation rate, and (e) the largest drop radius in

915 the S2 and M4 simulations.

916

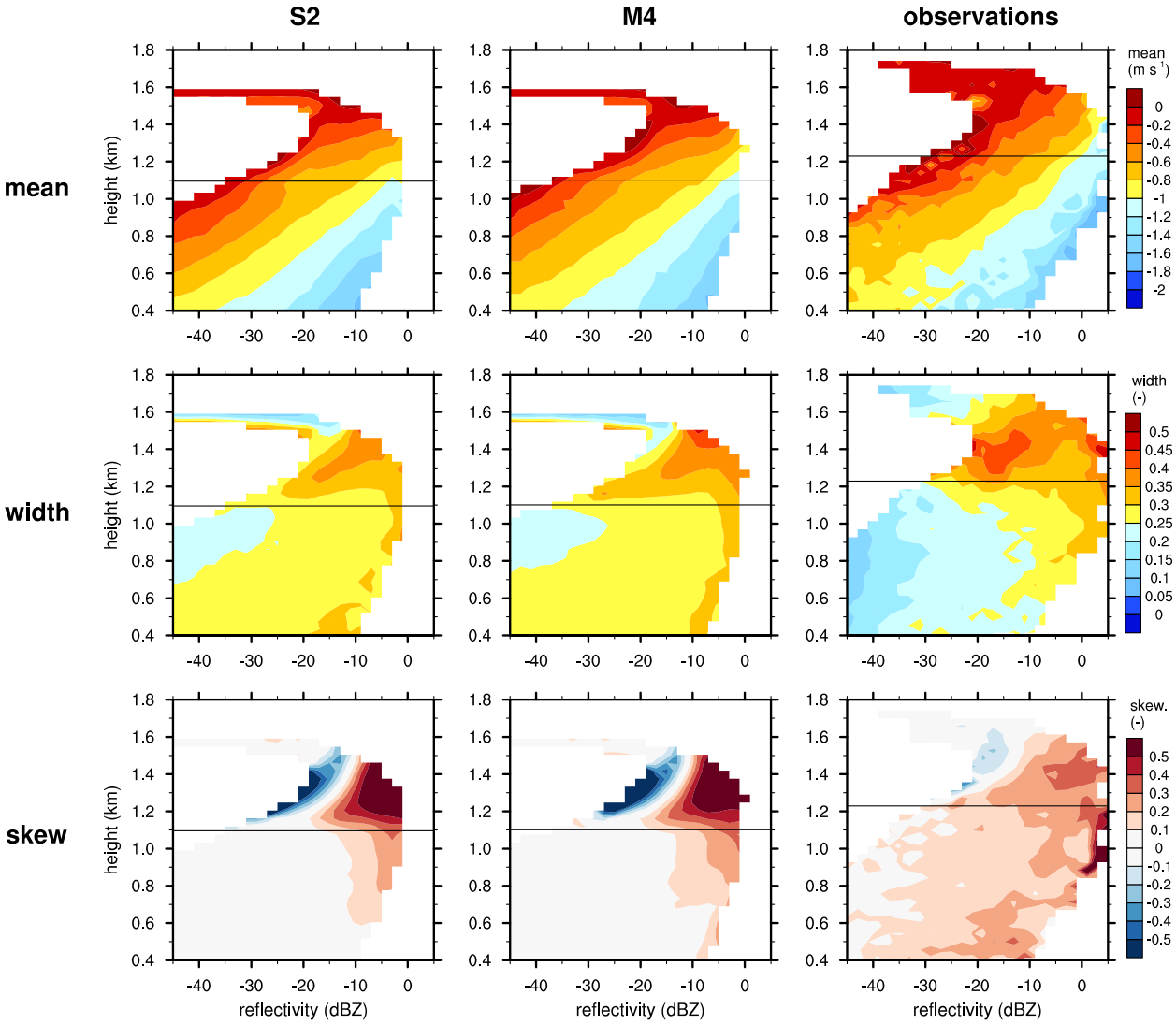


Fig. 15. Median of (top) mean Doppler velocity, (middle) width of Doppler spectra, and (bottom) skewness of Doppler spectra for a given radar reflectivity factor range and height obtained from (left) the S2 simulation, (center) the M4 simulation, and (right) observations. The sign convention for Doppler velocities is negative for downward motion. Black horizontal lines in the panels indicate the mean cloud-base heights.